Journal of Electroceramics 5:2, 153–182, 2000

Simulations of Composite Electrodes in Fuel Cells

SVEIN SUNDE
Institute for Energy Technology, P. O. Box 173, N-1751 Halden, Norway

Submitted January 27, 1999; Revised May 15, 1999; Accepted May 15, 1999

Abstract. Approaches to models and computer simulations of conductivity, polarization resistance, and impedance of composite electrodes in solid oxide fuel cells (SOFC) are reviewed with respect to the more important experimental findings. The approaches are classified according to how they model the highly disordered structure of composite SOFC electrodes: As corrugated layers of electrode material covered by a thin film of electrolyte or vice versa (thin film model), as a random packing of particles (Monte Carlo calculations), or using a macroscopic, averaged description of the disordered electrode structure (macroscopic porous-electrode model). Thin film models appear to be useful rationalizations of some experimental measurements of polarization resistance, but in the stricter sense fail to predict a number of important electrode characteristics. The Monte Carlo method, on the other hand, apparently meets with most of the more prominent experimental results reported so far, although some issues concerning parameter choices, among other things, remain to be resolved. The macroscopic porous-electrode theory may serve as a useful simplification of the Monte Carlo method, but with a more limited scope.

Modeling of composite electrodes for SOFC thus appears to have reached a level where it can be used for practical engineering applications. As an example of this, the rate of methane reforming at Ni-YSZ cermet anodes under current load is calculated using the framework of the macroscopic porous-electrode theory, modified to include non-linear kinetics and gas-phase diffusion. The reforming reaction is quite evenly distributed in the anode, and its overall rate is therefore strongly dependent on thickness. However, most of the electrochemical reaction is likely to occur in a region closer than 10 μm to the bulk electrolyte. For an anode thickness larger than this, the current-collector potential at a given current is by and large independent of thickness. The ratio between the rates of the reforming and the electrochemical reactions can therefore be balanced to a certain degree by optimizing thickness, without significant loss in cell power. In addition, cermet porosity, volume fraction of Ni and Ni-particle size, appears to have a moderate effect in controlling the rate balance, which will have to be manipulated within the constraints set by the requirement of percolation in the gas-phase and the Ni- and YSZ-networks.

Keywords: modeling, SOFC, internal reforming, cermet

Introduction

Fuel cells are efficient electrochemical converters of the availability of fuels directly to electrical energy without the use of equipment like steam generators, turbines and generators [1]. In a fuel cell, fuel and oxidant are separated by an electrolyte through which a current flows during oxidation of the fuel. Fuel cells are usually classified according to their operation temperature and the type of electrolyte employed. For example, the solid oxide fuel cell (SOFC) consists of a solid (usually) oxygen-conducting electrolyte sandwiched between electronically conducting anode and cathode layers, and operates at 800–1000°C [2,3]. Thermodynamically (among other things) there is an incentive to operate fuel cells at temperatures as low as possible. On the other hand, irreversible losses associated with current conduction and the electrochemical processes (polarization losses) dictates the temperature to be as high as possible. The resolution of this conflict is typically pursued by improving the electrical and electrochemical properties of cell

materials enough to operate the cell even at reduced temperatures without unacceptable polarization and ohmic losses. In state-of-the-art SOFC, compositionally uniform materials like yttria-stabilized zirconia (YSZ) and perovskite-type oxides like $La_{1-x}Sr_xMnO_3$ (LSM) are popular candidates for efficient electrolytes and cathodes, respectively [2,3]. For the anode, composites like Ni-YSZ cermets are usually chosen [2–16]. To allow for the species taking part in the electrochemical reactions to meet (i.e., electrons, electrolyte ions, and gas molecules), both the anode and cathode are usually porous.

The principal arguments for using composites at the anode side, were initially associated with stability and thermo-mechanical compatibility with the electrolyte [2]. However, in recent years the view that there may also be significant reduction and polarization losses by extension of the reaction zone for the electrochemical reaction is gaining widespread support [3,7,9,11,12,17–19]. As a consequence, composite cathodes (e.g., YSZ-LSM [20]) are also emerging as an attractive alternative to e.g., LSM. However, to keep losses at minimum, judicious design of the electrodes in terms of composite topology, morphology and composition is needed.

Computer models for composite electrodes for SOFCs may prove invaluable both in terms of understanding basic phenomena and ultimately for the quantitative design and optimization process itself. Depending on their mode of application, these models will need to meet certain validation criteria. First, they should reproduce as many of the salient characteristics of composite electrodes as possible, and with as high a degree of accuracy as possible. However, simplified models not in compliance with all experimental findings may in some cases still prove useful, provided that the limitations of the model are easily inferred from the assumptions made. Secondly, the model should be reasonably general, and preferably provide relations between microscopic parameters and macroscopic properties of the composite electrode. Of special interest in this context are relations between conductivity and polarization resistance on one hand, and porosity, morphology and structure on the other. Finally, simplicity of implementation and adaptability are considered valuable assets.

The purpose of this paper is to review some of the attempts to formulate a modeling framework for composite electrodes in SOFCs. We will evaluate these attempts with respect to the criteria advocated above. In view of the first of these, we will need to review what the salient experimental characteristics of composite electrodes are. This will be done in the section immediate to this one. As will become apparent from what follows below, the modeling process can be conceptually broken into the three tasks of (i) choosing a model structure for the composite, (ii) setting up current balances, and (iii) solving the resulting equations. We will base the classification of models here on the type of structure chosen, and in what follows after the next section describe thin-film models [17,18,21], models based on random packing of particles [19,22–24], and macroscopic porous-electrode theories [23,25,26] and in this sequence. (The nomenclature used here is in part our own, and not necessarily identical to that chosen by the authors of the papers quoted.) As it is our aim to show that modeling of composite SOFC electrodes have reached a level at which the use of these models in quantitative design applications may emerge as useful, we conclude this paper by applying the theory to judge the possibilities of steam-reforming methane internally in an SOFC.

Salient Experimental Features of Composite Electrodes for SOFC

We consider here composites consisting of a predominantly ionically conducting material (electrolyte material) and a predominantly electronically conducting material (electrode material), as most composites associated with SOFCs are of this type. Some important phenomena observed with such composite electrodes in SOFC and which have strong bearings on the optimum design of these are:

I. an apparently completely disordered structure, made up of particles of the electrode and electrolyte material uniform in extension and mixed at random [4–6,8,11,13,14,17,27–31]
II. a porosity often in the order of 30% (with some variations) [4,15]
III. an abrupt increase in conductivity with volume fraction Φ of the electrode material at a certain critical fraction Φ_c [2,4,15]
IV. a decrease in Φ_c with increasing ratio between electrolyte-particle radius a_{el} and electrode-particle radius a_{ed} [8]

V. a more or less abrupt decrease in conductivity with coarsening of the electrode particles [13]
VI. a relatively broad minimum in polarization resistance at intermediate Φ [5]. For $a_{ed}/a_{el} = 1$ the minimum often occurs around $\Phi = 0.4$–0.5 [32]
VII. a (strong) dependence of the minimum polarization resistance of a_{ed}/a_{el} [5b,16,32]
VIII. an increase in Φ at which the polarization resistance is minimum with decreasing a_{el}/a_{ed} [5]
IX. structure-dependent impedance spectra [6,9,11,12,32]. Also, in some cases impedance spectra change shape as a function of temperature: the higher the temperature, the more features become apparent in the spectra [20]
X. a marked thickness dependence of the polarization resistance at intermediate Φ; the larger the thickness the lower the polarization resistance, reaching an asymptotic limit at large thickness [17,18]
XI. at high values of Φ, the polarization resistance is thickness-independent [17].

Many of the findings on this list may be related solely to the topological arrangement of electrode and electrolyte clusters within the composite. Although these observations are reasonably clear-cut, many others made on composite SOFC electrodes show less convergence. These discrepancies may, in turn, be explained by differences in structure. Thus, it appears that models that take into account the effect of particle connectivity might be particularly useful in elucidating the properties of composite electrodes for SOFC. Nevertheless, the thin-film model described next demonstrate that a certain degree of insight can be obtained by simply making assumptions about this connectivity.

Thin-Film Models

The thin-film model is a model for polarization losses, and in some versions of the model also ohmic losses, in composite electrodes based on the assumption that all three phases of the electrode, i.e., electrolyte, electrode, and gas phases, form contiguous paths from bulk electrolyte to current collector. In the work of [17,18], the pores are modeled as straight channels of radius r in an electrode material. The channel surfaces are covered by a thin film of electrolyte material, and the model thus represents the very disordered structure of real electrodes (experimental observation I) by a very ordered structure. A current balance on this geometry is then performed, assuming linear electrochemical kinetics, which amounts to a one-dimensional differential current balance along the pores. Solution of the resulting pair of first-order differential equations yields for the polarization resistance R_p of the electrode

$$R_p = \sqrt{\rho k_i}\coth\sqrt{\rho L^2/k_i} \tag{1}$$

where ρ is the (empirical) resistivity of the electrolyte layer, k_i is equal to the product of an interfacial resistance k_i' and $r/2$ (to be obtained by fitting to experimental data), and L is the thickness of the electrode.

Instead of modeling the electrolyte as a the thin film, one may choose to treat the electrode material as the thin film, covering the surfaces of straight channels in the electrolyte material (connected to the bulk electrolyte) [21]. Also, the model can easily be extended to more than one dimension, and by adding thin film material to surfaces other than the pore walls, e.g., at the pore bottom for the case of the electrode material playing the role of a thin film [21]. The most important difference between these latter approaches and the original model proposed by Kenjo et al. [17] is that adding electrode material to pore bottoms causes R_p to remain finite as electrode thickness approaches zero (Eq. (1) diverges as $L \to 0$). (Other, less important differences are discussed in Tanner et al. [21]. Note, however, that Eq. (1) is not correctly reproduced in this reference.)

Due to the assumption of straight, connected strands of electrolyte and electrode material, the thin-film model is basically concerned with the current distribution in the electrode and does not address aspects of connectivity as such. Therefore, the model does not make predictions of phenomena obviously related to connectivity and particle size, such as observations III, IV, V, VI, VII, and VIII on the above list. Concerning observation XI, an apparent thickness independence of R_p may in general be caused either by the interfacial current being concentrated so closely to the composite's interface to the bulk electrolyte that R_p appears as thickness independent ($L^2 \gg k_i/\rho$ in Eq. (1)), or by breakdown of connectivity in either the electrode or electrolyte phases (see discussion below). The thin-film model

recognizes only current-distribution effects as causes for thickness-independence, and then only *a posteriori*. Also, some of the important parameters entering the model can not be easily related to independent measurements, notably for the interfacial resistance k_i', and serve as empirical parameters to be obtained by fitting. In spite of these shortcomings, the thin film model represents a useful conceptual framework for discussing (laterally averaged) current distributions in composite-fuel cell electrodes.

Although not explicitly making the assumption of straight pores and thin-films of electrolyte or electrode phases, the transmission line model of Kawada et al. [7] resembles the thin-film model of Kenjo et al. [17] in that it is a one-dimensional current balance based on the assumption of electrolyte and electrode particle connectivity. However, Kawada et al. [7] relaxes the approximation of linear electrochemical kinetics, and calculates non-linear current versus overpotential relationships, focusing on the effects of grain-boundary resistance in electrolyte particles. The (linear) impedance of the electrodes is also calculated, showing a strong dependence on the ratio between bulk and grain-boundary resistance of electrolyte particles. No extensive comparison with experimental results is presented in the paper, but as this approach is essentially the same as that of the thin-film model, so will its deficiencies be.

Models Based on Random Packing of Particles

The basic assumptions behind models based on random packing of particles are (1) that the composite electrode can be represented by discrete particles of electrolyte and electrode material packed together completely at random (experimental observation I), (2) that current is conducted from particle to particle through necks formed between them, and (3) that representative aggregates can be created on a computer either by serial, random deposition of spheres, leading to highly amorphous structures, or by regular lattices of a chosen structure, e.g., cubic [19,22–24] (see also e.g., [33–35]). Due to the randomness of this approach, the method is also frequently referred to as the Monte Carlo method [36]. The lattices are stored on the computer as lists of particle coordinates and their corresponding radius and type. Necks are created by allowing the radii of the spheres to increase in unison, removing overlapping material, until the desired porosity is obtained (experimental observation II) [22]. For example, for a cubic lattice of spheres, the porosity is $1 - \pi/6$. If one assumes all necks between particles i and j to be of the same circumference $l_{ij} = l$, and the particle radii are a_p, the porosity is

$$\varepsilon = 1 - \left\{ \frac{4}{3}\pi\Gamma^3 - \pi(\Gamma - a_p)\left[3\left(\frac{l}{2\pi}\right)^2 + (\Gamma - a_p)^2 \right] \right\} / (8a_p^3) \tag{2}$$

where $\Gamma = a_p / \cos[\tan^{-1}(l/2\pi a_p)]$. The particle radius a_p is here defined as the shortest distance from the particle center to the neck plane. Thus, if $1 = 3\,\mu$m and $a_p = 1\,\mu$m, the porosity is 31.7% according to this model (c.f. experimental observation II). For lattices with varying l_{ij} or for which the coordination number is different from that of cubic lattices (six), more complicated formulas will result, depending on the additional assumptions necessary in these cases.

Usually the particle packings are created in the form of sheets containing some thousands of particles, but even relatively small lattices (# particles $\sim$ 1000) can yield physically relevant information. Cyclic boundary conditions assure effectively infinite extension in the lateral directions [19,22–24]. Once the lattice has been generated, a list of neighboring particles is easily made from the list of particle coordinates and size [19,22–24].

In order to calculate the desired electrical and electrochemical properties of the electrodes, the Kirchhoff current law is now applied to every neighboring pair of particles on the list. Thus, for site i we have [19,22–24,35,36]

$$I_i = \sum_j I_{ij} = \sum_j (V_j - V_i)\sigma_{ij} \tag{3}$$

where I_i is the sum of currents I_{ij} going into lattice site i (zero for all internal sites in the composite), V_i and V_j the voltages at site i and j, respectively, and σ_{ij} the bond conductance between sites i and j. These quantities may in principle be real or complex, and time-dependent or not. Applying Eq. (3) to all sites in the lattice and with appropriate boundary conditions, yields a set of finite difference equations, for which efficient numerical methods of solution exist. The only thing that remains in order to relate the calculations to microscopic quantities, is the calcula-

tion of the bond conductances. The following approximation for a bond between two particles of the same material can be used [22–24,37]

$$\sigma_{ij} = \kappa_i l_{ij}/4 \tag{4}$$

whereas for two dissimilar particles,

$$\sigma_{eled} = \left[(2\sigma_{ed})^{-1} + (2\sigma_{el})^{-1} + \sigma_p^{-1}\right]^{-1} \tag{5}$$

is used [19,22–24]. Here, κ_i is the bulk conductivity of the electrode or electrolyte material, depending on whether Eq. (4) is applied to an electrode-electrode contact, or to an electrolyte-electrolyte contact, respectively. σ_{ed} is an electrode bond-conductance according to Eq. (4). σ_{el} is an electrolyte bond-conductance according to Eq. (4). σ_p is a polarization conductance, and is often measured and quoted with respect to the length of the so-called three-phase boundary (l_{TPB}), which is nothing but the length of the circumference of the electrode-electrolyte particle contact in the present model, [19,22–24,38] and references therein and the application section below. Again, all these quantities may be real, complex, and time dependent or not. The length of the neck circumferences needed in Eq. (4), can be estimated via Eq. (2) (or possibly its equivalents for other types of lattices) using some typical value for the electrode porosity.

Conductivity is usually measured at high frequencies to short capacitances contained in σ_p. For calculation of conductivity of the composite, therefore, $(\sigma_p)^{-1}$ is set to zero in Eq. (5) [19,22–24]. Polarization resistance is normally defined as the difference between the high- and low-frequency resistances of the electrode. Thus, for the evaluation of the polarization resistance of the composite, an additional calculation is needed, for which the low-frequency (constant) limit of σ_p is used. The polarization resistance is then calculated as the difference between the two. For intermediate frequencies, the electrode impedance is calculated using the frequency-dependent, complex expression for σ_p, and possibly also σ_{ed} and σ_{el} [24].

The merits of the random-packing model are illustrated in Fig. 1, in which conductivity v. volume fraction Φ of Ni in a 20 μm thick YSZ-Ni cermet as calculated from the random-packing model. All particle radii are 1 μm. The conductivity κ has been normalized with respect to that of Ni(κ_{ed}) at a temperature of 1000°C, and all other temperature-dependent parameters are those expected to be the most relevant for this temperature. Included in the figure are also three sets of experimental data from Dees et al. [4] and Ivers-Tiffe et al. [15]. Taking the scatter of the experimental results into account, the random-packing model appears to compare well with the measured values. In particular, the model predicts the large jump in conductivity at $\Phi \approx 0.3$ (experimental observation III).

Calculated polarization resistance R_p is shown in Fig. 2 for values believed to be typical for Ni-YSZ cermets (at 1000°C). Experimental results have not been included, since these tend to vary widely in magnitude. Nevertheless, the shape of the R_p versus Φ curve is similar to those obtained in experiments (experimental observation VI) [5]. The absolute magnitude of R_p is in reasonable agreement with the lowest values reported, but there is some uncertainty concerning the best combinations of σ_p and electrode-electrolyte circumference $l_{ed-el}(= l_{TBP})$ to be used. (For a closer discussion of this point, see Mogensen et al. [38] and Sunde [23].) In this context we note an alternative approach to the above one for representing porosity in composites, given by Abel et al. [39]. In their work, Abel et al. [39] randomly assigns a number of positions (corresponding to the desired porosity) in face-centered cubic lattices to voids. Only electrolyte-electrode contacts surrounded by a sufficient number of connected voids and where both particles are connected to their corresponding bulk phases are electrochemically active. All other electrolyte-electrode contacts are assigned an infinite resistance, as are all void-particle resistances. This approach inevitably leads to a smaller number of three-phase boundaries in the composite, which might explain any problem of too small polarisations resistances. However, as Abel et al. [39] unfortunately put little emphasis on comparison with experimental data, a ranking of this approach in terms of the criteria set forth in the introduction above is difficult. Nevertheless, we note that the percolation threshold of fcc lattices (≈ 0.2) may appear a bit low in comparison with most experimental results for composites of (approximately) uniform particle size, c.f. Fig. 1.

For conductivity and polarization resistance, the random packing model also survives comparison with experimental observations IV, V, VIII, X and XI given in the summary above. Of special importance is the fact that the model can predict the drop in

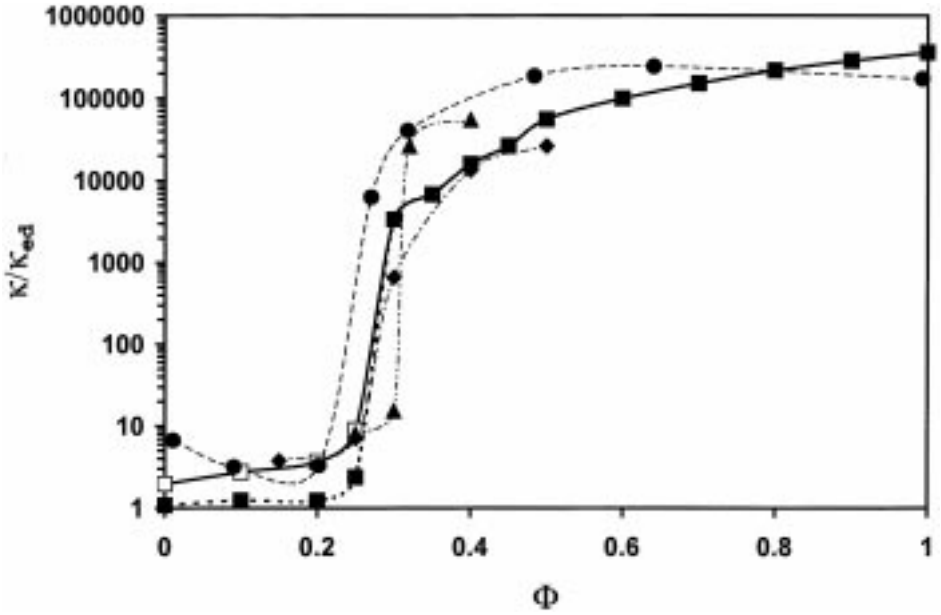

Fig. 1. Dimensionless conductivity κ/κ_{ed} as a function of volume fraction Φ of Ni in Ni-YSZ cermets calculated by the random packing method with $l_{TPB} = 3\ \mu$m (■) and $l_{TPB} = 0.3\ \mu$m (□). The thickness is 20 μm, all particle radii are 1 μm, all neck circumferences between electrode particles and between electrolyte particles are 3 μm, and the conductivity of Ni and ZYSZ are 2 10^4 S/cm and 0.1 S/cm, respectively. Experimental data from Ivers-Tiffee et al. (50% porosity data, ●) and Dees et al. (Zircar YSZ: ▲ , Toyo YSZ: ◆) are included.

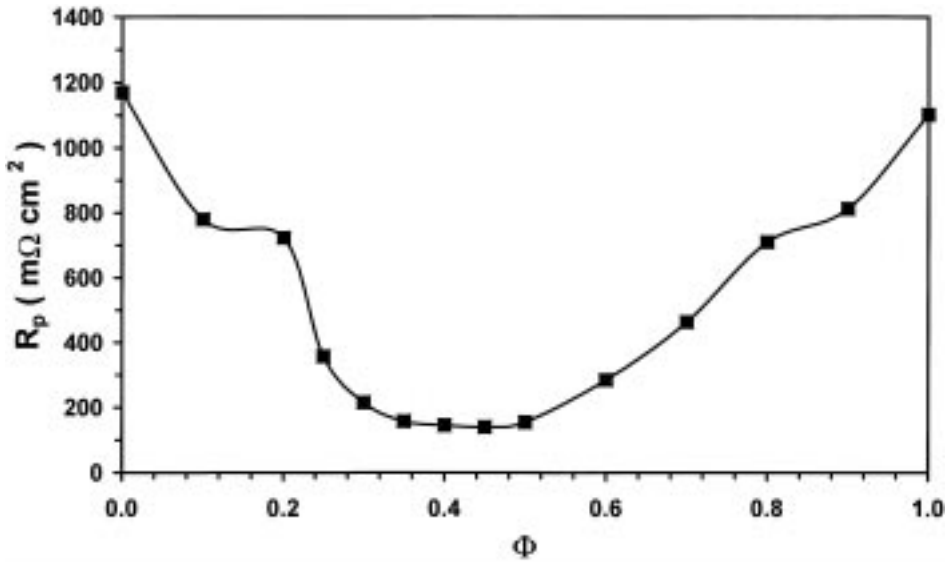

Fig. 2. Polarization resistance R_p as a function of volume fraction Φ of Ni in Ni-YSZ cermets calculated by the random packing method with $l_{TPB} = 3\ \mu$m, $\sigma_p = 10^{-4}$ S/cm, and all other parameters as in Fig. 1.

conductivity with Ni-particle aggregation in Ni-YSZ cermets (experimental observation V [13]). The model offers the explanation that this drop in conductivity is due to the increase in percolation threshold with increasing ratio between Ni and YSZ radii, thus pushing the conductivity ''over the edge'' [22]. Actually, this interpretation can be made on the basis of experimental observation IV alone, but was apparently first made in the context of the random-packing model. In addition, the temperature dependence of the conductivity of Ni-YSZ cermets calculated by the random-packing model is in quantitative agreement with experimental results [4]. Finally, the thickness dependence of R_p is also in accord with experimental results, and is qualitatively similar to that predicted by Eq. (1) above as long as the volume fraction of electrode particles is larger than Φ_c and the volume fraction of electrolyte particles is larger than their percolation threshold [23]. Outside this regime, there will be no thickness-dependence of R_P whatsoever the values of the other parameters of the model [23]. This is in contrast with Eq. (1), which can only explain an apparent absence of thickness dependence of R_p as due to a current distribution effect, i.e., as a trade-off between ohmic and polarization losses. The random packing approach, on the other hand, predicts that in addition to this trade-off effect the absence of thickness dependence can be caused by the absence of electrode or electrolyte clusters that has ramifications from one side of the electrode to the other, in accord with simple intuition.

The thickness dependence of R_p is discussed at length in Sunde [23], which also presents a ''phase diagram'' for which Φ regimes where a thickness dependence is possible or not as a function of $\alpha = a_{el}/a_{ed}$, see also Costamagna et al. [25]. (The reader may at this point want to note the unjustified claim made in Tanner et al. [21] about the Monte Carlo method that the thickness dependence of R_p is solely a ''statistical effect''. Also, note that in Sunde [23] the data by Kenjo et al. are quoted to display ''no thickness dependence for low Φ'', whereas it should read ''high Φ''. This is, however, of no consequence for the conclusions in that paper, since the thickness independence is predicted both for low and high values of Φ.)

Concerning experimental observation VII, measurements carried out in different laboratories are strongly diverging [5,16], and a comparison with calculations is not easy. Also, these measurements were carried out for much larger ratios of a_{el}/a_{ed} than has hitherto been simulated. In addition, the calculated results would depend very much on the choice of the neck widths in the composite. A shallow minimum in R_p at $a_{el}/a_{ed} = 1$ may be noticed for the parameters used in the calculations in Sunde [23], c.f. also Lee et al. [32], but no unequivocal conclusion can be made for the present concerning this point.

The impedance of random-packing models for composite electrodes has been treated extensively by Sunde [24], using a generic model for a three-step reaction as the interfacial impedance between electrode and electrolyte particles. An interfacial capacitance was also included for the complex version of σ_p. (The modulus of this impedance increases with decreasing frequencies, and, depending on the parameters, gives rise to one or more semicircles when plotted in an impedance-plane plot.) The basic result of these calculations is that the appearance of impedance-plane plots of the composite can be significantly different from those of the interfacial impedance alone. At the low frequency end of the spectrum, however, the impedance-plane plots remain undistorted in terms of shape.

The high-frequency distortions were shown to be due to enclaves of electrode material in percolating electrolyte clusters, i.e., electrode particles not connected to the current collector, in Sunde [24]. At low frequencies these confined electrode-particle regions are effectively blocked by the high impedance of the electrode-electrolyte interface which current would have had to surmount if it was to pass through them. As the frequency increases, however, the magnitude of this interfacial impedance drops, and the electrode enclaves do to an increasing degree conduct current. This effect therefore alters the current distribution in the electrode with frequency. The phenomenon is illustrated in Fig. 3.

As can be expected, the changes in current distribution with frequency are very dependent on electrode structure. Figs. 4 through 6 shows the impedance of a composite containing 50 volume percent electrode material, during electrode particle aggregation. In Fig. 4, the electrode and electrolyte particles have the same radius. In Fig. 5, the electrode-particle radius has increased to one and a half times that of the electrolyte-particle radius, and in Fig. 6 to

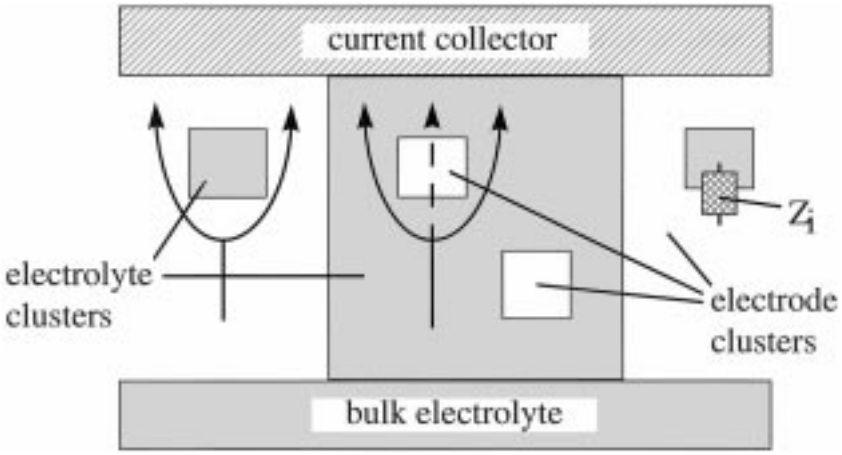

Fig. 3. Current distribution at low (solid arrows) and high frequency (dashed arrow) in a composite electrode. At low frequency the high interfacial impedance $Z_i(\omega)$ effectively blocks current from passing through highly conducting electrode-particle enclaves in sample-spanning electrolyte clusters. As the frequency increases $|Z_i(\omega)|$ drops, and the electrode enclaves do to increasing extent take part in current conduction. This distorts the high-frequency part of the impedance spectra [24]. The same is not true for electrolyte enclaves in sample-spanning electrode clusters, however, due to the (usually) much lower conductivity of the electrolyte.

two times that of the electrolyte-particle radius. The other parameters are as given in Fig. 4 of Sunde [24] along with the details of the interfacial impedance. The single-contact interfacial impedance appears in the impedance-plane plot for these parameters as a single semicircle.

It is worth noting the large increase in both ohmic resistance and polarization resistance of the composite

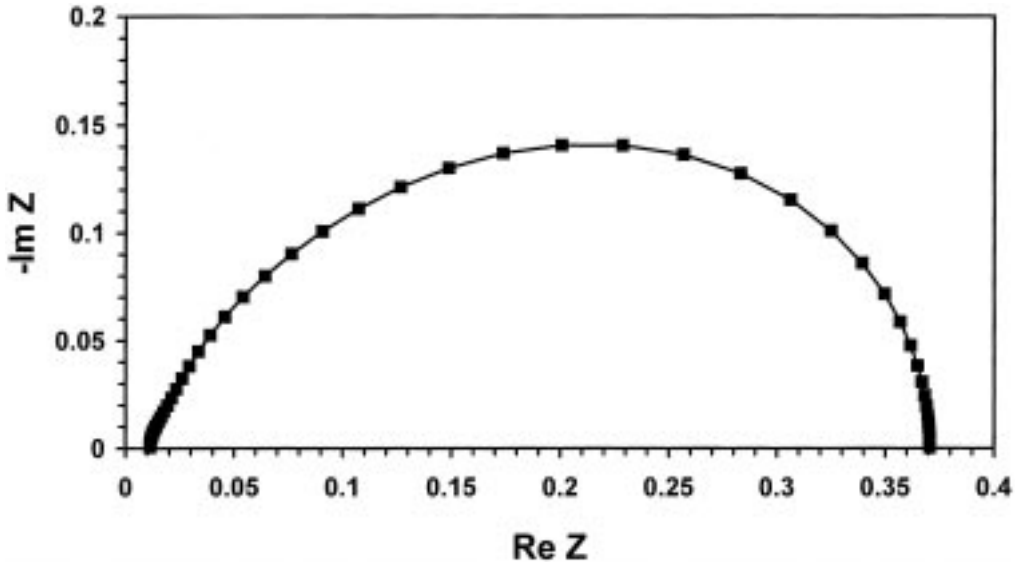

Fig. 4. Dimensionless impedance-plane plot calculated for a composite with $\Phi = 0.5$ and $\alpha = a_{el}/a_{ed} = 1$. All other parameters are as in Fig. 4 of Sunde [24], which also defines the dimensionless impedance and explains the model for the interfacial impedance corresponding to σ_p used.

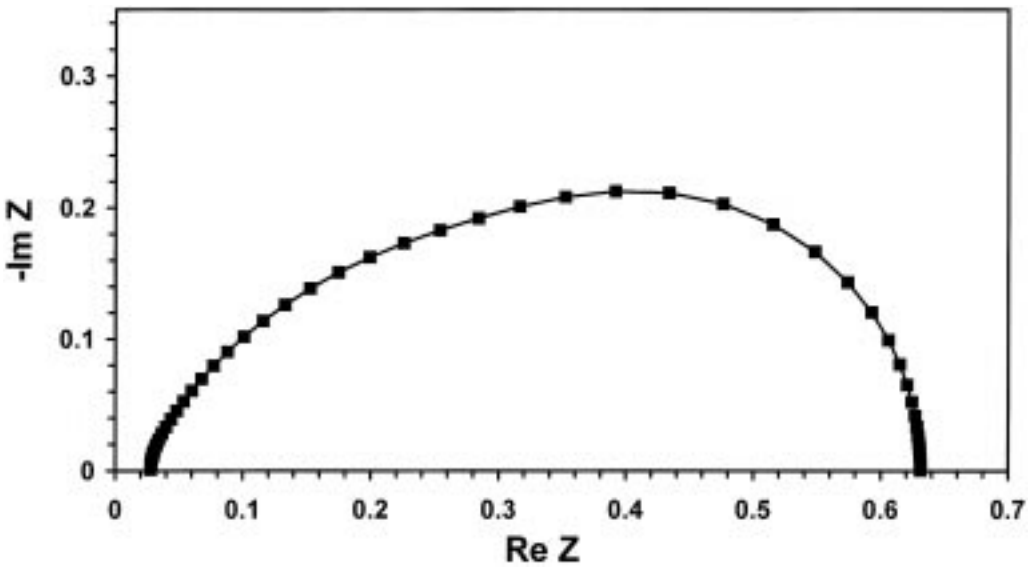

Fig. 5. Dimensionless impedance-plane plot calculated for a composite with $\Phi = 0.5$ and $\alpha = a_{el}/a_{ed} = 2/3$. All other parameters are as in Fig. 4 of Sunde [24], which also defines the dimensionless impedance and explains the model for the interfacial impedance corresponding to σ_p used.

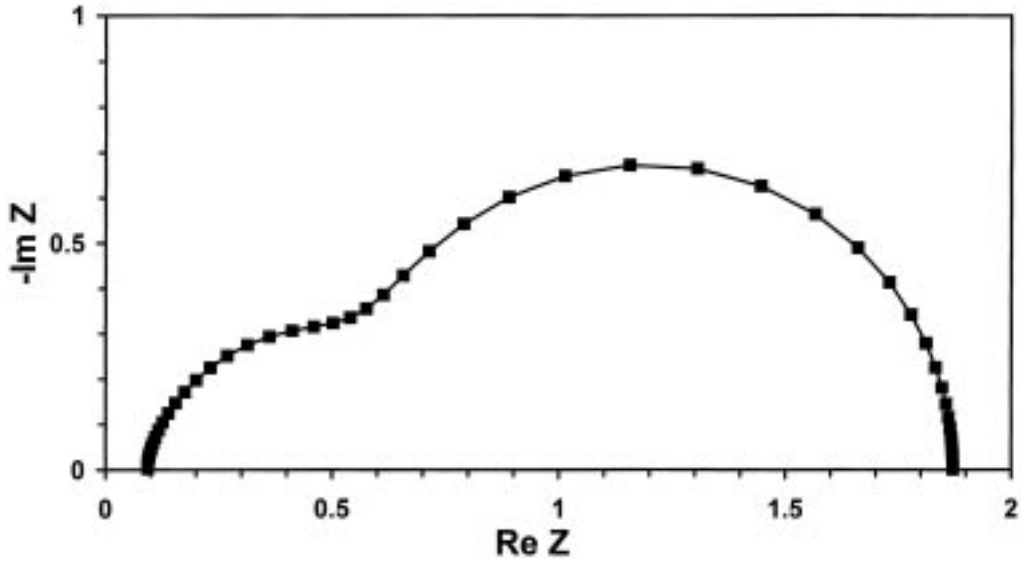

Fig. 6. Dimensionless impedance-plane plot calculated for a composite with $\Phi = 0.5$ and $\alpha = a_{el}/a_{ed} = 1/2$. All other parameters are as in Fig. 4 of Sunde [24], which also defines the dimensionless impedance and explains the model for the interfacial impedance corresponding to σ_p used.

electrode with decreasing ratio between the electrolyte particle radius and electrode particle radius $\alpha = a_{el}/a_{ed}$, Fig. 4 through 6. (Note the error in the symbol list in Sunde [23] and [24], where R, corresponding to α in the present paper, should be the ratio between electrolyte and electrode particle radius and not vice versa.)

The impedance calculations are difficult to verify by comparison with experimental data, simply because of the large scatter in the published experimental results. On the other hand, this scatter may itself be taken as an indication of justification of the predicted strong influence of structure on impedance data. Another difficulty is extrapolation of data for single-point electrodes to interfacial impedances as they occur in the composite. In some cases, however, there is (qualitative) agreement between the model and measurements. For example, the temperature-dependence of the shape of impedance-plane plots for composite cathodes reported by Juhl et al. [20] is similar to the corresponding ones calculated by Sunde [24].

Thus, with Eqs. (3) through (5) the conductivity, polarization resistance and impedance of the composite can be evaluated as a function of the conductivity of the constituent materials, σ_p, electrode structure (a_{ed}, a_{el}, l_{TPB}, l_{eded}, l_{elel} and lattice structure), electrode thickness, volume fraction of electrode material and porosity. In principle, the model therefore contains no free parameters. In practice, however, the porosity can vary quite a lot, and the neck circumferences are likely to be distributed around some mean value rather than all taking one single value. The mean values for the different types of necks (i.e., electrode-electrode, electrode-electrolyte, and electrolyte-electrolyte) may also be different. Finally, Eqs. (4) and (5) are approximations in two respects. First, at high frequencies they are better the shorter the l_{ij}, and for large neck circumferences l_{ij} might better be regarded as an effective neck circumference rather than its geometrical value. In addition, at low frequencies the current may be constricted to the close vicinity of the three-phase boundary (due to limited transport of reactants and products). If so, the assumption that the ohmic part of the resistance of an electrode-electrolyte contact is the sum of half the ohmic resistances of the corresponding homogeneous contacts (i.e., the terms $(2\sigma_{ed})^{-1}$ and $(2\sigma_{el})^{-1}$ in Eq. (5)) appears to break down [40,41]. (Actually, this assumption not exact even for a two-phase contact, since the primary and secondary current distributions are not the same [42a]. However, effects of current constriction are presumably to a large degree already included in the $(\sigma_p)^{-1}$-term of Eq. (5), since constriction is usually not corrected for in measurements of σ_p. Current-distribution effects may therefore not be the most significant cause for any inaccuracy of Eq. (5), at least for dc calculations.) All these factors work against the precise evaluation of l_{ij} via electrode porosity under all circumstances. The degree of agreement between porosity and conductivity in Fig. 1 is nevertheless somewhat reassuring.

Macroscopic Porous-Electrode Theories

Like models based on random packing of particles, two of the basic assumptions behind macroscopic porous-electrode theories are that the composite electrode can be represented by particles of electrolyte and electrode material packed together completely at random and that current is conducted from particle to particle through necks formed between them. However, instead of using computer-generated packing where all particle positions and types are known, macroscopic theory disregards the actual geometric details of the composite. Instead, the electrode is described in terms of continuous, average quantities, in analogy with corresponding theory for single-phase porous electrodes used in aqueous electrochemistry [42b].

Although porous-electrode adaptations to composite electrodes in principle could be made three-dimensional, all results presented so far have been for one-dimensional formulations. The average electric potential in the composite is thus assumed to vary continuously in the direction normal to the electrode plane in the macroscopic porous-electrode model. Only clusters of electrolyte particles and electrode particles extending through the entire composite are taken into account. Separate current balances for the electrode and electrolyte clusters form a set of differential equations for the potentials and currents in the electrolyte and electrode clusters using effective media expressions for their conductivity [23,25]. This set of differential equations is then solved with constant-current boundary conditions [23,25]. Linear expressions are used for the kinetics of the electrochemical reaction [23,25]. From this, the total (low-frequency) electrode resistance can be calculated analytically. The resistance corresponding to the high-frequency resistance can be calculated by use of e.g.,

effective medium equations [43], the polarization resistance emerging as the difference between these two resistances.

For the effective conductivities of electrolyte and electrode clusters, percolation thresholds for these clusters are needed. These thresholds can be obtained as a function of particle size (and possibly modified for finite-size scaling [36]) from coordination-number theories [44–46] (see application section below), or Monte Carlo or even experimental results can be used. The other parameters of the model can be estimated in various ways from microscopic quantities [23,25].

Since only sample-spanning electrolyte and electrode clusters are included in the macroscopic porous-electrode model, the theory will not be valid outside the Φ-regime in which clusters of this type are present, i.e., below Φ_c or at volume fractions of electrolyte particles $f = 1 - \Phi$ below their percolation threshold f_c. Outside this range, the theory is not applicable [23]. Also within the limits $\Phi = \Phi_c$ and $\Phi = 1 - f_c$ the results should be used with some caution, however. In fact, the expression for the electrode resistance diverges at both these percolation thresholds, and we do not recommend any firm conclusions to be drawn from calculations made very close to the percolation thresholds [25]. Nevertheless, at intermediate Φ, which are those associated with the greatest engineering interest, the macroscopic theory gives very good agreement with the results of Monte Carlo simulations [23]. This result holds also for thin electrodes, thus rebutting the impression one may get from the work of Costamagna et al. [25] that the theory is valid only for large ratios of thickness to particle radius. The Φ-range for which it does provide accurate results is expected to be somewhat dependent on thickness, but this exact dependence has not yet been sorted out, c.f. [23,25].

When used with coordination number theories for particle packings, the macroscopic porous-electrode theory agrees with all relevant observations on the list presented above, except again maybe experimental observation VII.

Further details about the macroscopic theory can be found in the section below on internal steam-reforming of methane, where a non-linear version of it that also includes the effects of gas-phase transport is presented. However, before concluding this section we would like to make one final point: In analogy with aqueous electrochemistry [42b], the difference between single-pore models such as the thin-film model and macroscopic models appears to lie primarily in the interpretation and/or calculation of parameters. In both cases the differential equations to treat are the same, c.f. Kenjo et al. [17] and Sunde [23]. We have here nevertheless made a distinction between these two approaches due to the fact that aspects of connectedness of electrode and electrolyte clusters have not yet been taken into account in the thin film models. All phases are simply *assumed* to be contiguous. This makes in our opinion a very significant difference from the macroscopic approach in which one calculates conductivties etc. from relationships that do take the degree of contiguity of clusters into account, c.f. the application section below.

Summary of Models

The three different approaches to modeling of composite electrodes in SOFC are compared with respect to the experimental observations listed in the section on salient experimental features above in Table 1. Although observation I is not something predicted by the models but would rather be more appropriately listed as a model assumption, it is included in the table to highlight the differences between the theories. The prediction concerning porosity is taken to be fulfilled if porosity enters the model directly or indirectly as an independent parameter, and if a porosity in the order of 30% makes the model predict other measurable quantities in agreement with their experimental values, e.g., conductivity. The column for the macroscopic porous-electrode theory in Table 1 has been filled in assuming that percolation thresholds are calculated using coordination-number theories [44–46] for percolation thresholds.

From Table 1, the Monte Carlo model appears to represent the type of approach that best predicts the most important experimental features of composite electrodes. Its range of applicability is also larger than the other two. In terms of quantitative agreement with polarization resistance and conductivity, all three models are apparently of equal rank. However, one should not disregard the fact that whereas the thin-film model contains free parameters (film resistivity and charge-transfer conductance), in the other two models the free parameters (neck circumferences) are constrained to also be compatible with a measurable quantity (porosity), at least for low values of l_{ij}.

In terms of simplicity, the macroscopic porous-electrode theory and the thin film models are clearly

Table 1. Comparison of models of composite electrodes for SOFC. Theoretical predictions in agreement with experimental observations are indicated by a $\surd$ symbol

Experimental observations	Thin film	Monte carlo	Porous electrode
I		$\surd$	$\surd$
II		$\surd$	$\surd$
III		$\surd$	$\surd$
IV		$\surd$	$\surd$
V		$\surd$	$\surd$
VI		$\surd$	$\surd$
VII			
VIII		$\surd$	$\surd$
IX		$\surd$	
X	$\surd$	$\surd$	$\surd$
XI	$(\surd)$	$\surd$	

superior to the Monte Carlo approach. Also, the Monte Carlo approach does not lend itself easily to the introduction of phenomena that are best treated on a continuum basis, e.g., gas-phase diffusion, in the model.

In summary then, the basic phenomena occurring in composite SOFC electrodes are best studied by the Monte Carlo method. The porous-electrode model may, however, with regard to its simplicity and its ability to assess its own range of applicability, emerge as the most practical method for applied research. We illustrate this point in the next section.

Application: Internal Steam Reforming of Methane in SOFC

Internal reforming of natural gas at the anode of an SOFC [2] to form species more electrocatalytically active than e.g., methane, is expected to simplify system design and to improve the thermodynamic efficiency of the cell with respect to operation on externally reformed gas [47]. The overall amount of electrochemically produced heat is more than enough to balance the overall energy required for the endothermic reforming reaction [48,49]. However, unless the reforming and electrochemical reactions occur at comparable rates locally, large temperature gradients in the cell may result [48–50], among other things giving rise to intolerable mechanical stresses. Recent data indicate that the reforming reaction proceeds at a rate of roughly $5\,\mathrm{mol}\,h^{-1}\,g_{Ni}^{-1}$ at a cermet composed of Ni and YSZ under a partial pressure of methane of 0.25 atm and at 1000°C [51]. If we assume a porosity of 35%, a volume fraction of Ni of 50% with respect to all solid material, and all particle radii to be equal, a $50\,\mu$m thick cermet contains $1.5 \cdot 10^{-2}\,g_{Ni}\,\mathrm{cm}^{-2}$. Under a current load of $100\,\mathrm{mA\,cm}^{-2}$, the ratio χ between the reforming rate and the electrochemical reforming rate (converted to $\mathrm{mol\,h}^{-1}$) at this cermet would be in the order of 50. It therefore appears that a balancing of the two reactions is within reach, by a careful optimization of the electrode structure. Such a balancing would require a knowledge of effects due to mass transfer and coupling between the electrochemical and reforming reactions neglected in this rough estimate, however. Also, one might have to pay for a better balancing of the two reactions in terms of increased overvoltage of the electrode, corresponding to a loss in cell power.

In order to facilitate the design of electrode structures capable of balancing the rates of the reforming and electrochemical reactions, we develop here a mathematical model for internal reforming at an SOFC Ni-YSZ anode with concurrent electrochemical reaction based on the macroscopic porous-electrode approach. Our purpose is to demonstrate that significant reduction in χ may be achieved with negligible loss in overpotential by optimizing cermet thickness, to discuss other, microstructural means to the same end, and as stated above demonstrate a practical application of the macroscopic porous-electrode theory. After formulation of the theory and a discussion of parameter choices, results will be presented and discussed in terms of feasibility of internal reforming of methane at conventional Ni-YSZ anodes.

Physical Description and Assumptions

A gas mixture of hydrogen, methane, water vapor, carbon monoxide and carbon dioxide is led past the composite electrode at constant flow rate and a total pressure of $p^0 = 1$ atm. The gas mixture results from pre-reforming of methane with steam at an initial steam-to-carbon ratio S/C, and a subsequent shift reaction

$$CH_4 + H_2O \rightleftarrows CO + 3H_2 \tag{6}$$

$$CO + H_2O \rightleftarrows CO_2 + H_2 \tag{7}$$

The pre-reforming is allowed to proceed until a given fraction Δ of the methane initially present has reacted according to Eq. (6), before the exposure to the composite anode.

A steady-state current is passed through the electrode. We want to calculate the distribution of partial pressures and rates of chemical and electrochemical reactions within the electrode, as functions of current and gas composition. To assess the effect of a change in anode thickness or a microstructural parameter on power loss of the fuel cell, we also want to calculate the potential at the current collector relative to that in the bulk electrolyte close to its interface to the anode. We make the following assumptions in addition to those underlying the macroscopic porous-electrode theory (vide supra):

1. The electrode under test is small enough that there are no gradients in the transverse directions in partial pressures, temperature etc.
2. Reactant and product gases are transported through voids left between the particles, and no portions of the composite are sufficiently dense that this gas- phase transport is blocked. There are no significant variations in porosity in the anode.
3. All gases behave according to the ideal gas law.
4. Gas-phase transport is adequately treated by Fick's law of diffusion with constant diffusion coefficients [52]. The gas flow-rate is sufficiently high that no partial pressure outside the anode is influenced by the reactions occurring inside the anode.
5. The electrode material in the anode catalyses reactions (6) and (7), whereas the current-collector and the electrolyte are catalytically inactive for reforming and shift.
6. The shift reaction is always at equilibrium.
7. The rate of electrochemical oxidation of species other than H_2 is at the partial pressures present under operating conditions negligible with respect to that of the latter [3,53–56]. The polarization resistance for a contact between an electrode and electrolyte particle is inversely proportional to the three-phase boundary between the gas-phase and the two solid phases, l_{TPB} [10,57–60]. The reaction proceeds according to

$$H_2 + O_o^x \rightleftarrows H_2O + V_o^{\bullet\bullet} + 2e' \tag{8}$$

where O_O^x and $V_O^{\bullet\bullet}$ are (in Kröger-Vink notation) an oxygen atom and an oxygen vacancy in the YSZ lattice, respectively. e' is an electron picked up by the current collector.

8. The electrocatalytic properties of the electrode-electrolyte interfaces in the composite and its catalytic activity for steam-reforming are independent of one another [56]. That is, we assume all rate constants to be independent of partial pressures. Gas-phase reactions do not proceed at any significant rate.
9. The anode operates isothermally.
10. Local variations in the open-circuit potential are negligible.

Basic Equations

Under the assumptions above, we may write for the current density i_{ed} flowing through the electrode cluster and the current density i_{el} flowing through the electrolyte cluster [23]

$$i_{ed} = -\kappa_{ed}^* d\varphi_{ed}/dx \tag{9}$$

$$i_{el} = -\kappa_{el}^* d\varphi_{el}/dx \tag{10}$$

and

$$di_{ed}/dx + di_{el}/dx = 0 \tag{11}$$

where φ_{ed} and φ_{el} are the potentials in the electrode and electrolyte clusters. (The current densities i_{ed} and i_{el} are averages over the entire cross-sectional area of the electrode.) The clusters have effective conductivities κ_{ed}^* and κ_{el}^*, and the two first relations are expressions for Ohm's law. The last relation expresses charge conservation. For the current transferred from an (percolating) electrode cluster to a (percolating) electrolyte cluster, we write [6]

$$di_{el}/dx = \lambda_{TPB} i_0 [\exp(\beta_a \eta_s) - \exp(-\beta_c \eta_s)] \tag{12}$$

where $\eta_s = \varphi_{ed} - \varphi_{el} - U'$ (U' is the open-circuit potential), and the parameters β_a and β_c have the units of reciprocal potential. In Eq. (12), i_0 plays the role of an exchange current density given with respect to TPB length, in view of assumption (7). Thus, λ_{TPB} is the three-phase boundary per volume in the anode. We take i_0 to depend on the partial pressures of hydrogen and water as

$$i_0 = \left(\frac{p_2}{p_2^0}\right)^{\gamma_2} \left(\frac{p_4}{p_4^0}\right)^{\gamma_4} i_0(p_2^0, p_4^0) \tag{13}$$

where p_2 and p_4 are the partial pressures of water vapor and hydrogen, respectively, and p_4^0 and p_2^0 are reference pressures. (We assign for the following subscript $i = 1$ to CH_4, $i = 2$ to H_2O, $i = 3$ to CO, $i = 4$ to H_2, and $i = 5$ to CO_2, following their order of appearance in Eqs. (6) and (7) above.) The parameters γ_2 and γ_4 are apparent reaction orders with respect to the partial pressures of water vapor and hydrogen, respectively.

For all species, the material balance reads at steady state and in one dimension,

$$-\frac{d\,N_i}{dx} + R_i = 0 \tag{14}$$

where N_i is the molar flux of species i relative to stationary coordinates and averaged over the entire cross-section of the electrode, and R_i is the rate of production (in mol cm^{-3} s^{-1}) of species in chemical and electrochemical reactions. According to assumptions 3 and 4 above,

$$N_i = -\frac{D_i^e}{RT}\frac{dP_i}{dx} \tag{15}$$

where R is the gas constant, T the temperature, p_i the partial pressure of species i, and $D_i{}^e$ the effective diffusion coefficient of species i in the gas mixture in the pores of the composite anode.

Denoting the rate of reactions (6) and (7) r_I and r_{II}, respectively, both normalized with respect to surface area of catalyst (electrode material) (mol cm^{-2} s^{-1}), we may write

$$R_1 = -ar_I \tag{16}$$

$$R_2 = -ar_1 - ar_{II} + \frac{1}{2F}\frac{di_{el}}{dx} \tag{17}$$

$$R_3 = ar_I - ar_{II} \tag{18}$$

$$R_4 = 3ar_I + ar_{II} - \frac{1}{2F}\frac{di_{el}}{dx} \tag{19}$$

and

$$R_5 = ar_{II} \tag{20}$$

where a is the surface area of electrode particles per volume in the anode (cm^{-1}). The last terms in Eqs. (17) and (19) are production of water and consumption of hydrogen, respectively, due to reaction (8) above. For the rate of the reforming reaction (6), we will use [47]

$$r_I = k\left(p_I - \frac{p_3 p_4^3}{K_I p_2}\right) \tag{21}$$

where k is a rate constant (mol cm^{-2} s^{-1} atm^{-1}) and K_I is the equilibrium constant for reaction (6). From assumption 6),

$$p_5 = \frac{K_{II} p_2 p_3}{p_4} \tag{22}$$

where K_{II} is the equilibrium constant for reaction (7) above. Sufficient boundary conditions for the coupled Eqs. (9) through (22) are given by

$$i_{el} = -I, i_{ed} = 0, \varphi_{el} = 0, N_i = 0; \quad x = 0 \tag{23}$$

and

$$i_{el} = 0, p_i = p_i^s; \quad x = L \tag{24}$$

where L is the thickness of the composite electrode and $x = 0$ corresponds to the interface between the composite anode and the bulk electrolyte [23,42b,61]. I is the superficial current density, and p_i^s is the partial pressure of species i at $x = L$.

Analysis

By integrating Eq. (11) using the first and second of the boundary conditions in Eq. (23), we may combine Eqs. (9) and (10) to give

$$\frac{d\eta_s}{dx} = -i_{ed}\left(\frac{1}{\kappa_{ed}^*} + \frac{1}{\kappa_{el}^*}\right) - \frac{I}{\kappa_{el}^*} \tag{25}$$

where we have set $U' = 0$. (That is, the potential is measured with respect to a reference electrode of the same kind. See also assumption 10.) Introducing the dimensionless parameters

$$y = x/L, \quad \nu^2 = \frac{\beta_a \lambda_{TPB} i_0 L^2 (p^0)^{(\gamma_2+\gamma_4)}}{(p_2^0)^{\gamma_2}(p_4^0)^{\gamma_4}}\left(\frac{1}{\kappa_{ed}^*} + \frac{1}{\kappa_{el}^*}\right),$$

$$\beta = \frac{\beta_c}{\beta_a} \tag{26}$$

and in addition using dimensionless partial pressures $\xi_i = p_i/p^0$, where p^0 is the total pressure at $x = L$, and dimensionless potential $\phi = \beta_a \eta_s$, Eq. (25) may be differentiated and the result combined with Eqs. (12) and (13) to read in dimensionless form

$$\frac{d^2\phi}{dy^2} - \nu^2 \xi_2{}^{\gamma_2} \xi_4{}^{\gamma_4}\left(e^{\phi} - e^{-\beta\phi}\right) = 0 \tag{27}$$

Reactions (6) through (8) give three independent stoichiometric relations for five unknown partial pressures. Three dependent variables are therefore enough to describe the system, and the other two can be obtained by implicit relations. We choose here p_1, p_2 and p_5 as the independent variables, and note that from Eqs. (14) and (16) through (20) we may write

$$\frac{dN_3}{dx} = -\frac{dN_1}{dx} - \frac{dN_5}{dx} \tag{28}$$

and

$$\frac{dN_4}{dx} = -2\frac{dN_1}{dx} - \frac{dN_2}{dx} \tag{29}$$

Introduction of Eq. (15) into Eqs. (28) and (29), and use of the boundary conditions Eqs. (23) and (24), allow Eqs. (28) and (29) to be solved to give partial pressures p_3 and p_4 as a function of p_1 and p_5, and p_1 and p_2, respectively [62]. On dimensionless form, Eqs. (9) through (22) and the solutions of Eqs. (28) and (29) can be combined to give the following set of equations

$$\frac{d^2\xi_1}{dy^2} - \pi_{11}\xi_1 + \pi_{12}\xi_3\xi_4^3\xi_2^{-1} = 0 \tag{30}$$

$$\frac{d^2\xi_2}{dy^2} - \pi_{21}\xi_1 + \pi_{22}\xi_3\xi_4^3\xi_2^{-1} + \pi_{23}\frac{d^2\xi_5}{dy^2} + \pi_{24}\frac{d^2\phi}{dy^2} = 0 \tag{31}$$

$$\xi_3 + \pi_{31}\xi_1 + \pi_{32}\xi_5 = \xi_3{}^s + \pi_{31}\xi_1^s + \pi_{32}\xi_5^s \tag{32}$$

$$\xi_4 + \pi_{41}\xi_1 + \pi_{42}\xi_2 = \xi_4^s + \pi_{41}\xi_1^s + \pi_{42}\xi_2^s \tag{33}$$

and

$$\xi_5 - K_{II}\xi_2\xi_3\xi_4^{-1} = 0 \tag{34}$$

Here, $\xi_i{}^s$ denote the value of ξ_i at $x = L$, i.e., $p_i{}^s/p^0$. In Eqs. (30) through (34), we have also introduced the dimensionless variables

$$\pi_{11} = akRTL^2/D_1^e \tag{35}$$

$$\pi_{12} = akRTL^2(p^0)^2/K_I D_1^e \tag{36}$$

$$\pi_{21} = akRTL^2/D_2^e \tag{37}$$

$$\pi_{22} = akRTL^2(p^0)^2/K_I D_2^e \tag{38}$$

$$\pi_{23} = D_5^e/D_2^e \tag{39}$$

$$\pi_{24} = \frac{RT}{2F\beta_a D_2^e p^0}\left(\frac{1}{\kappa_{ed}^*} + \frac{1}{\kappa_{el}^*}\right)^{-1} \tag{40}$$

$$\pi_{31} = D_1^e/D_3^e \tag{41}$$

$$\pi_{32} = D_5^e/D_3^e \tag{42}$$

$$\pi_{41} = 2D_1^e/D_4^e \tag{43}$$

and

$$\pi_{42} = D^e{}_2/D_4^e \tag{44}$$

(K_{II} in Eq. (34) is already dimensionless). Finally, by the use of the dimensionless current δ and the conductivity ratio κ,

$$\delta = \beta_a IL\left(\frac{1}{\kappa_{ed}^*} + \frac{1}{\kappa_{el}^*}\right), \quad \kappa = \frac{\kappa_{el}^*}{\kappa_{ed}^*} \tag{45}$$

we may write the boundary conditions on dimensionless form as

$$\frac{d\xi_1}{dy} = \frac{d\xi_2}{dy} = 0; \quad y = 0 \tag{46}$$

$$\xi_1 = \xi_1^s, \quad \xi_2 = \xi_2^s; \quad y = 1 \tag{47}$$

$$\frac{d\phi}{dy} = -\frac{\delta}{\kappa + 1}; \quad y = 0 \tag{48}$$

$$\frac{d\phi}{dy} = \delta - \frac{\delta}{\kappa + 1}; \quad y = 1 \tag{49}$$

Method of Solution

The set of nonlinear Eqs. (27) and (30) through (34), of which Eqs. (27), (30) and (31) are differential equations with boundary conditions (46) through (49), constitute a well-defined problem once the dimensionless constants and cell current δ are specified. The equations are solved by linearizing around a trial solution, and the resulting linear equations solved by Newman's BAND subroutine, as outlined in Newman [42c]. The calculations are then repeated using the solution obtained as the new trial solution, until convergence. An appropriate trial solution for ϕ is obtained by linearizing Eq. (27) with respect to ϕ, using $\xi_2 = \xi_2{}^s$ and $\xi_4 = \xi_4{}^s$, and solving the resulting

second-order differential equation with respect to ϕ with boundary conditions (48) and (49).

Current-collector Potential

In order to calculate the measured current-collector potential, $\varphi_{ed}(x=L)$, from η_s, we need to evaluate $\varphi_{el}(x=L)$. A second-order differential equation for $\varphi_{el}(x)$ can be obtained by differentiating Eq. (10) and combine the result with Eq. (12). One gets

$$\beta_a \frac{d^2\varphi_{el}}{dy^2} + \frac{\nu^2}{\kappa+1}\xi_2^{\gamma_2}\xi_4^{\gamma_4}\left(e^{\phi} - e^{-\beta\phi}\right) = 0 \tag{50}$$

which may be solved using the result for η_s, ξ_2, and ξ_4 found above. Boundary conditions are implicitly given by Eqs. (10), (11), (23) and (24), and Eq. (50) is also conveniently solved using the BAND-routine. $\varphi_{ed}(x=L)$ is then found as $\eta_s - \varphi_{el}(x=L)$.

For an analytical approximation to $\beta_a\varphi_{ed}(L)$, the trial solution for ϕ (see above) may be combined with the linearized version of Eq. (50) and associated boundary conditions. The result is given in Sunde [23] and Newman [42b], and may with the present dimensionless parameters be written as

$$\beta_a\varphi_{ed}(L) = \frac{\delta}{2+\kappa+1/\kappa}\left[1 + \frac{2+(\kappa+1/\kappa)\cosh\sqrt{\nu^2(1+\beta)(\xi_2^s)^{\gamma_2}(\xi_4^s)^{\gamma_4}}}{\sqrt{\nu^2(1+\beta)(\xi_2^s)^{\gamma_2}(\xi_4^s)^{\gamma_4}}\sinh\sqrt{\nu^2(1+\beta)(\xi_2^s)^{\gamma_2}(\xi_4^s)^{\gamma_4}}}\right] \tag{51}$$

Estimation of Constant Parameters

If the pores in the anode are much smaller than the mean free path of the diffusing species, the diffusion process will be dominated by molecule-wall interactions, whereas in bulk diffusion molecule-molecule interactions are important. For YSZ-cermets, a typical average pore diameter is in the order of 1 μm [63], which corresponds roughly to the mean free path of e.g., methane at 1000°C. For this transition regime, we therefore evaluate the diffusion coefficient from [52]

$$D_i^e = \left(\frac{1}{D_{i,m}^e} + \frac{1}{D_{i,k}^e}\right)^{-1} \tag{52}$$

$$D_{i,m}^e = \frac{1}{(1-x_i)}\sum_{j=1,j\neq i}^{n} D_{ij}^e x_j \tag{53}$$

$$D_{i,k}^e = \frac{4}{3}K_0\left(\frac{8RT}{\pi M_i}\right)^{1/2}; \quad D_{ij}^e = \frac{\varepsilon}{\tau}D_{ij}^0 \tag{54}$$

where D_{ij}^0 is the binary diffusion coefficient for a gas mixture of species i and j, D_{ij}^e an effective diffusion coefficient for a binary mixture of i and j in a porous medium of porosity ε and tortuosity τ, $D_{i,k}^e$ the Knudsen diffusion coefficient of species i multiplied by ε/τ, M_i the molecular mass of species i, $D_{i,m}$ the effective diffusion coefficient of species i in a multicomponent gas mixture, and x_i the mole fraction of species i. K_0 is a proportionality factor dependent on the pore radius (Knudsen coefficient), which we will set equal to 10^2 cm m^{-1} $r(\varepsilon/2\tau)$ (c.f. Veldsink [52] and Solheim [64]). Typical values for ε and τ are 0.3 [4] (experimental observation II) and 3, respectively. Values for M_i are found in standard tables to give $D_{i,k}^e$ for $i = 1,\ldots,5$.

Values for D_{ij}^0 at the temperatures under consideration here (1000°C), are obtained by extrapolating the low-temperature values in Bossel [65] by the procedures indicated in Bird et al. [66]. Thus,

$D_{12}^0 = 8.4\,\text{cm}^2\text{s}^{-1}$, $D_{13}^0 = 3.1\,\text{cm}^2\text{s}^{-1}$,
$D_{14}^0 = 9.8\,\text{cm}^2\text{s}^{-1}$, $D_{15}^0 = 2.5\,\text{cm}^2\text{s}^{-1}$,
$D_{23}^0 = 8.1\,\text{cm}^2\text{s}^{-1}$, $D_{24}^0 = 27.4\,\text{cm}^2\text{s}^{-1}$,
$D_{25}^0 = 6.6\,\text{cm}^2\text{s}^{-1}$, $D_{34}^0 = 10.5\,\text{cm}^2\text{s}^{-1}$,
$D_{35}^0 = 2.3\,\text{cm}^2\text{s}^{-1}$, $D_{45}^0 = 9.1\,\text{cm}^2\text{s}^{-1}$

may serve as typical values (in addition, $D_{ij}^0 = D_{ji}^0$).

For the effective conductivities κ_{ed}^* and κ_{el}^* above we will use [23]

$$\kappa_{ed}^* = (\kappa_{ed}l_{eded}/8a_{ed})[1-(1-\Phi)/(1-\Phi_c)]^t \tag{55}$$

and

$$\kappa_{el}^* = (\kappa_{el}l_{elel}/8a_{el})[1-\Phi/(1-f_c)]^t \tag{56}$$

where Φ is the volume fraction of electrode particles taken with respect to all solid. The parameter t is an empirical one, for which we will use the value 1.7 [22,23,43]. In Eq. (55), Φ_c is the percolation threshold for electrode clusters, as above. In Eq. (56), f_c again is the minimum volume fraction of electrolyte particles needed for the presence of an electrolyte cluster spanning from $x=0$ to $x=L$, i.e., the analog of Φ_c. The circumference of necks formed between electrode particles is denoted l_{eded}, and l_{elel} is used for the neck circumference of electrolyte-electrolyte necks. The

radii of electrode and electrolyte particles are still a_{ed} and a_{el} respectively ($l_{eded}, l_{elel}, a_{ed}$ and a_{el} are all assumed monodisperse). The factors $l_{eded}/8a_{ed}$ and $l_{elel}/8a_{el}$ are introduced in an attempt to correct for porosity, and the details of how they are arrived at can be found in Sunde [22]. As the assumptions behind the factors $\kappa_{ed}l_{eded}/8a_{ed}$ and $\kappa_{el}l_{elel}/8a_{el}$ in Eqs. (55) and (56) may break down for the large neck peripheries that would result for very low porosities (*vide supra*), these factors are replaced by the bulk conductivities κ_{ed} and κ_{el}, respectively. We will indicate below whenever this is the case.

We now explain the use of coordination number theories for calculating the percolation thresholds f_c and Φ_c. As in Sunde [23] and Bouvard and Lange [44], these are obtained via the coordination numbers Z_{elel} and Z_{eded}. Z_{elel} is the average number of electrolyte-particle neighbors that an electrolyte particle has in a random particle packing. Z_{eded} is the average number of electrode-particle neighbors of an electrode particle. We thus assume that f_c and Φ_c may be associated with universal critical coordination number Z^c_{elel} and Z^c_{eded} [44], both equal to 2.0 at the percolation threshold, i.e., $Z^c_{elel} = 2.0$ at $f = f_c$ and $Z^c_{eded} = 2.0$ at Φ_c [44]. Z_{eded} and Z_{elel} will be calculated from the coordination-number theory by [44], according to which

$$Z_{jk} = Z_j p_k Z_k / Z_t \tag{57}$$

where j and k refer to particle type, and both can be ''ed'' or ''el''. If $k =$''ed'', p_k is equal to the number fraction of electrode particles p. If $k =$''el'', p_k is the number fraction of electrolyte particles, equal to 1-p. The coordination numbers Z_{ed} and Z_{el} for the total number of neighboring particles of electrode and electrolyte particles, respectively, in Eq. (57), may be calculated from

$$Z_{ed} = 3 + (Z_t - 3)/[p + (1-p)\alpha^2] \tag{58}$$

and

$$Z_{el} = 3 + \alpha^2(Z_t - 3)/[p + (1-p)\alpha^2] \tag{59}$$

The number fraction of electrode particles p is found from

$$p = \Phi/[\Phi + (1-\Phi)/\alpha^3] \tag{60}$$

Z_t is the total average coordination number, taken here to be equal to six [44], and α is the ratio between the radius a_{el} of electrolyte particles and the radius a_{ed} of electrode particles. With $\Phi = \Phi_c$ when $Z_{eded} = Z^c_{eded} = 2.0$ and $1 - \Phi = f_c$ when $Z_{elel} = Z^c_{elel} = 2.0$, Eqs. (57) through (59) can be combined to give Φ_c and f_c.

For interfaces between percolating electrolyte and electrode clusters, the total TPB length per volume, λ_{TPB}, is proportional to the TPB length per contact between an electrode and an electrolyte particle $l_{edel} = l_{TPB}$, to the number of electrode particles per volume n, to the average number of electrolyte particles that each of these electrode particles contact Z_{edel}, and the probability that both the participating particles in an electrode-electrolyte contact are also connected to both bulk phases. We therefore write

$$\lambda_{TPB} = l_{TPB} \cdot n \cdot Z_{edel} \cdot P_c(Z_{eded}) \cdot P_c(Z_{elel}) \tag{61}$$

In Eq. (61), $P_c(Z_{eded})$ and $P_c(Z_{elel})$ are the probabilities that electrode particles and electrolyte particles are a part of electrode and electrolyte clusters, respectively, spanning from one side of the composite to the other [44],

$$P_c(Z_{ij}) = [1 - (2 - Z_{jj}/2)^{2.5}]^{0.4} \tag{62}$$

where $j =$''ed'' or ''el''. Z_{eded} and Z_{elel} will be calculated from Eqs. (57), (58) and (59). n in Eq. (61) can be found from

$$n = B\Phi/(4\pi a^3_{ed}/3) \tag{63}$$

which follows from assuming a constant relative density B for the composite when all the particle volumes are taken to be those of spheres. The relative density is defined here as the volume of all particles divided by the total volume of the composite. B may be taken to be equal to 0.6 [22,33,67,68].

Note that the assumed presence of two percolating clusters in the calculations above corresponds to $1 - \Phi > f_c(\alpha)$ and $\Phi > \Phi_c(\alpha)$ [23].

Table 2 summarizes some parameter values or ranges assumed to be relevant for typical Ni-YSZ anodes. For parameters depending on temperature, the values at 1000°C are given. In the table, what we will refer to as parameter set (a) below, are given in parentheses for those parameters for which ranges are indicated. The effective conductivities, the diffusion coefficients and λTPB, which are obtained indirectly from the equations above, are not given, however.

The range for the rate constant for Eq. (6) has been obtained indirectly. Belyaev et al. [56] quotes an Arrhenius-type of rate constant with a preexponential of $2.6 \cdot 10^9 \mu\text{mol min}^{-1}$ $(\text{vol}\%\ \text{CH}_4)^{-1}\ \text{g}^{-1}$ for

Ni-ZrO_2-CeO_2 electrodes containing 93% Ni. Converting this to an area-specific value by assuming a mean Ni-particle radius of 1 μm and spherical particles, and changing the other units to those used here, gives a value of roughly 10^{-2} mol s^{-1} cm^{-2} atm^{-1}. (If we approximate the surface area of Ni by that of an assembly of spheres of radius a_{ed}, the area of Ni per area of anode is $3LB\Phi/a_{ed}$.) With an activation energy of 162 kJ mol^{-1} [56], this amounts to a rate constant k of $2 \cdot 10^{-9}$ mol s^{-1} cm^{-2} atm^{-1}. A similar calculation for the data of Ødegård et al. [51] gives at 1000°C a rate constant k approximately equal to $2.1 \cdot 10^{-6}$ mol s^{-1} cm^{-2} atm^{-1}. (In the latter work, the reaction order with respect to methane is 1.2. Here, we have neglected this difference, and simply used the numerical value of the preexponential in Ødegård et al. [51] in the units of mol s^{-1} cm^{-2} atm^{-1}.) Using a Ni-radius of 1 μm and in addition assuming a porosity of 35%, the preexponential of Achenbach and Riensche [47] for Ni-YSZ cermets with 20 wt % Ni may be converted to $5 \cdot 10^{-3}$ mol s^{-1} cm^{-2} atm^{-1}. The activation energy in the latter work is 82 kJ mol^{-1}, giving $k = 2.2 \cdot 10^{-6}$ mol s^{-1} cm^{-2} atm^{-1}, in reasonable agreement with Ødegård et al. [51]. For our present purposes, we will use the range of rate constants shown in Table 2.

The specific exchange-current i_0($p^0_{H2} = 0.97$ atm, $p^0_{H2O} = 0.03$ atm) has been estimated from the specific polarization conductances κ_p in the table by assuming that the relation $\kappa_p = i_0(\beta_a + \beta_c)$ holds [6]. There appears to be no agreement in the literature concerning apparent reaction orders with respect to water and hydrogen, but i_0 appears to be less sensitive towards the pressure of the latter than towards the water-vapor pressure. However, both positive and negative values for both γ_2 and γ_4 are indicated in the literature [3,9,59,73–76].

For large porosities, the specific surface area a (cm^{-1}) may be estimated via Eq. (63), again assuming the surface areas of the particles to be roughly that of spheres (as for porosity). The mean pore diameter, used in the calculation of diffusion coefficients, can easily be estimated by considering a cubic lattice in which the radii of the initially spherical particles are increased beyond the lattice constant, truncating overlapping regions [78] (*vide supra*). The average pore radius of the narrowest part of pore throats is then

Table 2. Parameters for Ni-YSZ anodes for SOFCs. The values for the temperature-dependent parameters are given for a temperature of 1000°C. Numbers in parentheses following ranges are values corresponding to parameter set a

Parameter	Value	Ref.
a	$3 \cdot 10^3 - 9 \cdot 10^3$ cm^{-1}($9 \cdot 10^3$ cm^{-1})	
r	0.02 – 0.5 μm(0.5 μm)	
L	1 – 100 μm(50 μm)	[2,6,7,64,69]
κ_{ed}	$2 \cdot 10^4$ S cm^{-1}	[70]
κ_{el}	0.1 S cm^{-1}	[29]
l_{TPB}/a_{ed}	3 – 6(3)	[19,22,23,]
$l_{eded}/a_{ed}, l_{elel}/a_{el}$	3 – 6(3)	[19,22,23]
a_{ed}	0.1 – 5 μm(1 μm)	[4,69]
a_{el}	0.1 – 40 μm(1 μm)	[4,6,69]
Φ	0.4 – 0.5(0.5)	
t	1.7	[22,23,43]
$\kappa_p(p_{H_2}{}^0 = 0.97$ atm, $p_{H2O}{}^0 = 0.03$ atm)	$10^{-6} - 10^{-3}$ S cm^{-1}(10^{-4} S cm^{-1})	[10,38,57,71]
$i_0(p_{H_2}{}^0 = 0.97$ atm, $p_{H2O}{}^0 = 0.03$ atm)	$4 \cdot 10^{-8} - 4 \cdot 10^{-5}$ A cm^{-1} ($4 \cdot 10^{-6}$ A cm^{-1})	
k	$10^{-9} - 10^{-6}$ mol s^{-1} atm^{-1} cm^{-2} (10^{-6} mol s^{-1} atm^{-1} cm^{-2})	[47,51,56]
K_I	$9.225 \cdot 10^3$ atm^2	[72]
K_{II}	0.5864	[72]
γ^2	$<0 - 1(1)$	[52,73–76]
γ^4	$-1/2 - 1/2(0)$	[52,73–76]
β_a, β_c	2F/RT,F/RT	[60,77]

roughly equal to the lattice constant minus the radius of the particle-particle contact (neck) area, which can be calculated from neck circumferences l_{TPB}, l_{eded} and l_{elel}. Since the latter can also be related to porosity, Eq. (2), porosity and pore radius are therefore correlated. For $\varepsilon = 0.3$, r is in the order of 0.5 a_{ed} for a cubic lattice, and for $\varepsilon = 0.04$, which is close to the percolation threshold for gas-phase transport in cubic and random packings [78], r is in the order of 0.02 a_{ed} for a cubic lattice. We will take these estimates to be valid also for a random packing. For porosities of 4%, we reduced the specific surface area a by a factor of three with respect to that for porosities of 30%, to take into account the larger particle-particle interface areas. Also, l_{TPB} roughly doubles.

Results

In Fig. 7 is shown dimensionless potential at the current collector, $\beta_a \varphi_{ed}(L)$, as a function of dimensionless current for four different parameter sets as given in the caption. Curve a corresponds to parameter set a (Table 2). In curve b, the reaction order with respect to water has been changed to -0.5. ν^2 has been changed accordingly to 4.47 (ν^2 changes with γ_2 and γ_4, if i_0 at $p^0_{H2} = 0.97$ atm and $p^0_{H2O} = 0.03$ atm is kept constant, Table 2). In curve c, γ_4 has been set to 0.5, with a concomitant change in ν^2 to 873.4. In all of these calculations $S/C = 2$ and $\Delta = 0.05$. A calculation with the latter changed to 0.5 for the same parameter set as a is given in curve d of Fig. 7. The range for δ corresponds roughly to the current range 0 through 1 A cm^{-2}. The linear solution for $\beta_a \varphi_{ed}(L)$, Eq. (51), with parameters corresponding to curve b, is also shown in the figure. As apparent from the Fig. 7, for parameter set b, the linear solution, Eq. (51), is a reasonable approximation to the full solution only at the lower currents ($\delta > 2$, corresponding approximately to 80 mA cm^{-2}). (For the numerical calculations, $\beta_a \varphi_{ed}(L)$ was ascertained to vary as the square of the step length used in the calculations, as it should with the discretization

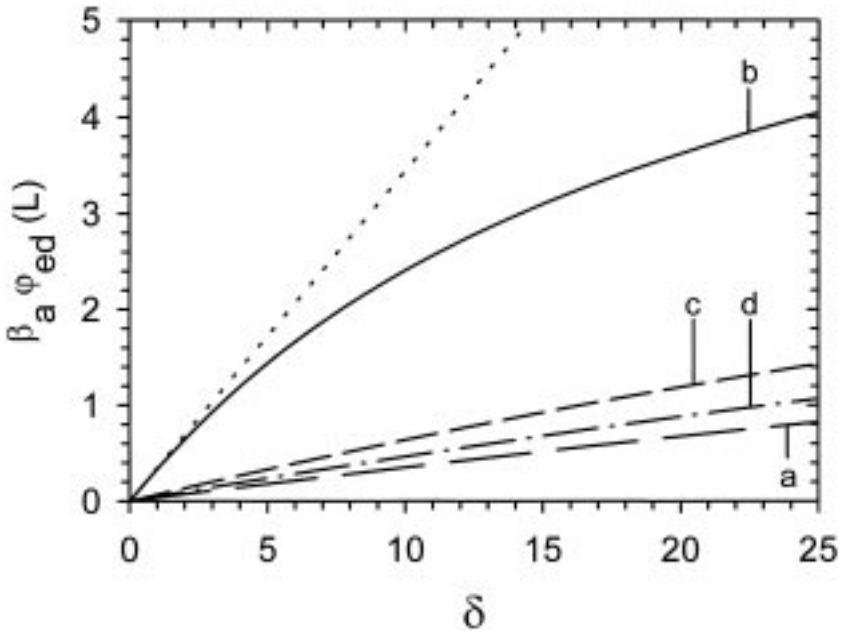

Fig. 7. Dimensionless potential at the current collector, $\beta_a \varphi_{ed}(L)$, as a function of δ. Parameters: a $\pi_{11} = 8.235 \cdot 10^{-2}$, $\pi_{12} = 8.927 \cdot 10^{-7}$, $\pi_{21} = 7.824 \cdot 10^{-2}$, $\pi_{22} = 8.481 \cdot 10^{-7}$, $\pi_{23} = 5.882 \cdot 10^{-1}$, $\pi_{24} = 3.511 \cdot 10^{-4}$, $\pi_{31} = 1.303$, $\pi_{32} = 8.068 \cdot 10^{-1}$, $\pi_{41} = 7.340 \cdot 10^{-1}$, $\pi_{42} = 3.863 \cdot 10^{-1}$, $K_{II} = 0.5864$, $\beta = 0.5$, $\kappa = 5 \cdot 10^{-6}$, $\nu^2 = 860.2$, $\gamma_2 = 1$, and $\gamma_4 = 0$. b $\gamma^2 = -0.5$ and $\nu^2 = 4.47$. All other parameters as in a. For this calculation, the linear solution Eq. (51) is also shown (short dashes). c $\gamma_4 = 0.5$ and $\nu^2 = 873.4$. All other parameters as in a. d Same parameters as in a. Partial pressures at $y = 1$ corresponds to $S/C = 2$ and $\Delta = 0.05$ for curves a, b, and c, and $S/C = 2$ and $\Delta = 0.5$ for curve d.

procedure used here [42b].) For the other curves a, c and d, the corresponding linear solutions, Eq. (51), were in good agreement up to much higher currents, typically $\delta \leq 15$, corresponding to 600 mA cm^{-2}. At currents higher than this, the numerically calculated $\beta_a \varphi_{ed}(L)$ were less than the linear solutions, Eq. (51), also for these parameter sets.

In Fig. 8 is shown the dimensionless electrochemical reaction rates (current distribution), dj/dy, where $j = i_{ed}/I$, at $\delta = 2$ for the same parameter sets as in Fig. 7. In addition, the current distribution for parameter set a at $\delta = 25$ is shown as curve e. The distribution of reforming reaction rate, $\rho_I = d^2\xi_1/dy^2$, is shown in Fig. 9 for parameter set a at $\delta = 2$. Whereas the reforming-reaction rate is higher closest to $y = 1$, the electrochemical reaction is for all parameter sets except b confined to a region close to the bulk electrolyte at $y = 0$. The reforming is quite evenly distributed over the entire anode, however, compared to the usually much stronger position dependence of the electrochemical reaction rates.

The total rate of reforming according to reaction (6) is equal to N_1 at $x = L$. (This may be realized by integrating Eq. (14) for $i = 1$ with respect to x from $x = 0$ to $x = L$, and using the boundary condition $N_1(x = 0) = 0$, Eq. (23).) With Eqs. (15), (35), (37), (40) and (45), one may write for the absolute value of the ratio of the total reforming rate (in mol cm^{-2} s^{-1}) to the total electrochemical reaction rate I/2F (mol cm^{-2} s^{-1}), χ,

$$\chi = \left|\frac{N_1}{I/2F}\right| = \frac{\pi_{21}}{\pi_{11}\pi_{24}\delta}\left(\frac{d\xi_1}{dy}\right) \tag{64}$$

For the parameter sets in Fig. 7, $d\xi_1/dy$ at $y = 1$ was, to within the convergence accuracy, independent of δ and equal to $2.45656 \cdot 10^{-2}$. For $\delta = 2$, Eq. (64) gives $\chi = 33.24$, that is $|I/2F| \ll |N_1|$. In line with this and the weak y-dependence of ρ_I, the partial pressures ξ_1 through ξ_5 are not very dependent on y, as shown in Fig. 10 for parameter set a at $\delta = 2$.

At $\delta = 25$ the distribution of reforming reaction-rate, ρ_I, was identical to that at $\delta = 2$. With $\delta = 25$,

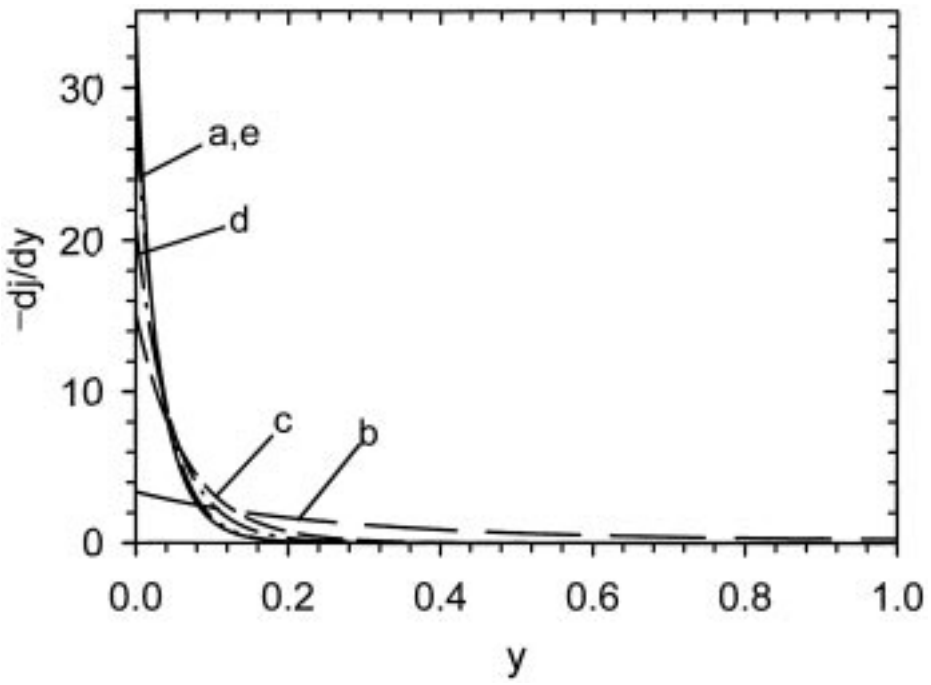

Fig. 8. Reduced current distribution at $\delta = 2$. Parameters are the same as in Fig. 7 for corresponding letters. In addition, the current distribution for $\delta = 25$ for the parameter set in a, Fig. 7, is shown as curve e.

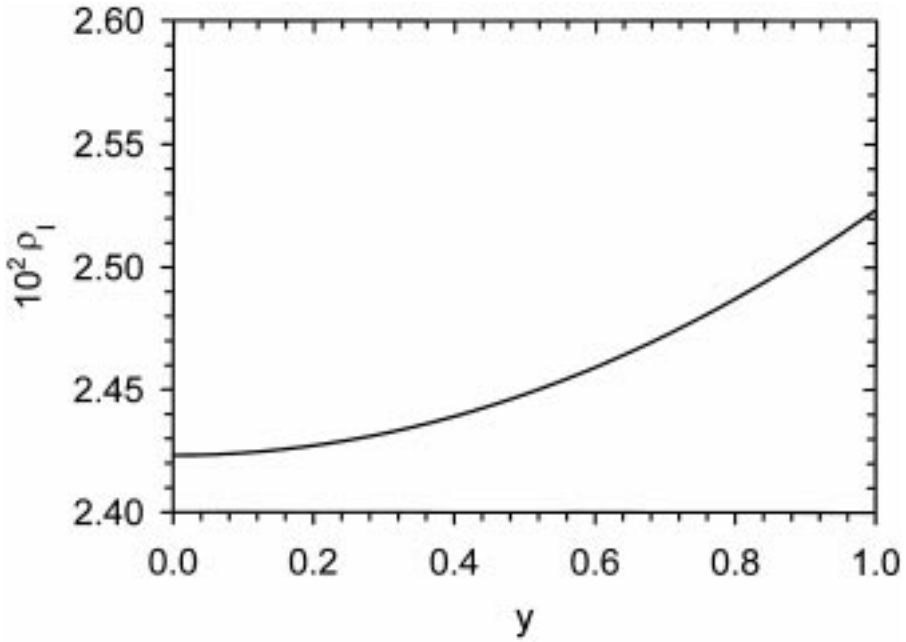

Fig. 9. Reduced distribution of rate of reaction (6) at $\delta = 2$. Parameters are the same as for curve a in Fig. 7.

χ now becomes 2.65, and a slightly higher partial pressure ξ_2 at $y = 0$ therefore appeared than at $y = 0$ in Fig. 10 due to the electrochemical production of water vapor. Also, ξ_4 was lower at $y = 0$ at $\delta = 25$ than at $\delta = 2$, due to the consumption of hydrogen in reaction (8). However, the effect of the electrochemical reaction on the partial pressures ξ_2 through ξ_4 was barely noticeable even at these high current densities, and ξ_1 did not appear to be affected at all. Figure 11 shows the partial-pressures versus y for $\Delta = 0.5$ at $\delta = 2$ for parameter set a. At these ξ_i^s, there are almost no pressure variations along the anode. In all the cases treated above, the total pressure along the anode varied less the 1% of p^0. The small deviations from p^0 that were present, were always positive.

In Fig. 12 is shown variations in χ with L for several parameter sets. Curve 1 corresponds to parameter set a. In curve 2, the volume-fraction of Ni, Φ, has been reduced to 0.4. This has consequences for λ_{TPB} and a via Eq. (63), and both of these were reduced by a factor 4/5 corresponding to the reduction in Φ. The conductivities κ_{ed}^* and κ_{el}^* are similarly affected via Eqs. (55) and (56), see also Fig. 1. In curve 3 of Fig. 12 is demonstrated the effect of reducing the porosity to 4%. For this calculation, the prefactors of Eqs. (55) and (56) were replaced by bulk conductivities as indicated above, and the lower ranges for a and the higher for l_{TPB} of Table 2 were employed. Likewise, when calculating the diffusion coefficients, r of 0.02 μm was used. In curve 4 of Fig. 12, the radius of the electrode particles, a_{ed}, has been increased to 2 μm with respect to the standard case, which reduces the specific surface area at $\Phi = 0.5$ by a factor of 0.5 with respect to parameter set a, and λ_{TPB} roughly by a factor of 0.4. Effective conductivities are again affected via f_c and Φ_c as in Eqs. (55) and (56). While the curves 1 through 4 are calculated using $\Delta = 0.05$, curve 5 demonstrates the effect of partial pressures at $x = L$ on the χ versus L curve. In Fig. 12, all curves except the low-porosity case appear to be almost linear. (For thickness-dependence calculations, it is convenient to introduce new dimensionless quantities, since many of those used so far depend on L. Thus one may keep constant π_{11}/δ^2, π_{12}/δ^2, π_{21}/δ^2, π_{22}/δ^2 and ν^2/δ^2, rather than π_{11}, π_{12}, π_{21}, π_{22}, and ν^2, respectively. δ may then serve as dimensionless thickness for given current, Eq. (45), since no other dimensionless parameters depend on L if this replacement is made. Also, we may express Eq.

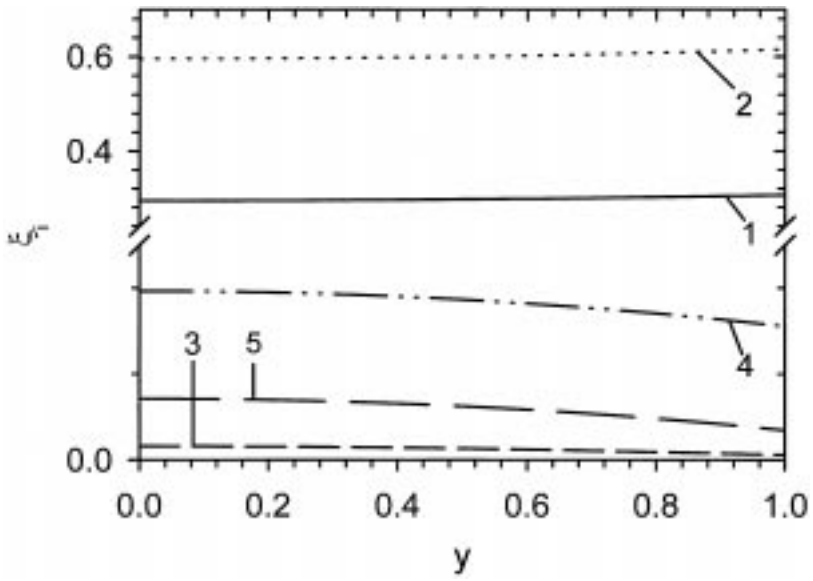

Fig. 10. Dimensionless partial pressures at $\delta = 2$. Parameters are the same as curve a in Fig. 7.

(64) in terms of π_{11}/δ^2 and π_{21}/δ^2 by multiplying both numerator and denominator by δ^2.)

In Fig. 12, while thickness is crucial in determining χ, the effect of Φ, of the electrode-particle size, and of ε is more moderate. (Although the porosity may appear to be significant in reducing χ, a porosity of $\varepsilon = 0.04$ must be considered quite extreme in the present context (experimental observation II), and possibly not obtainable in practice in a well-controlled manner.) In spite of this, the current-collector

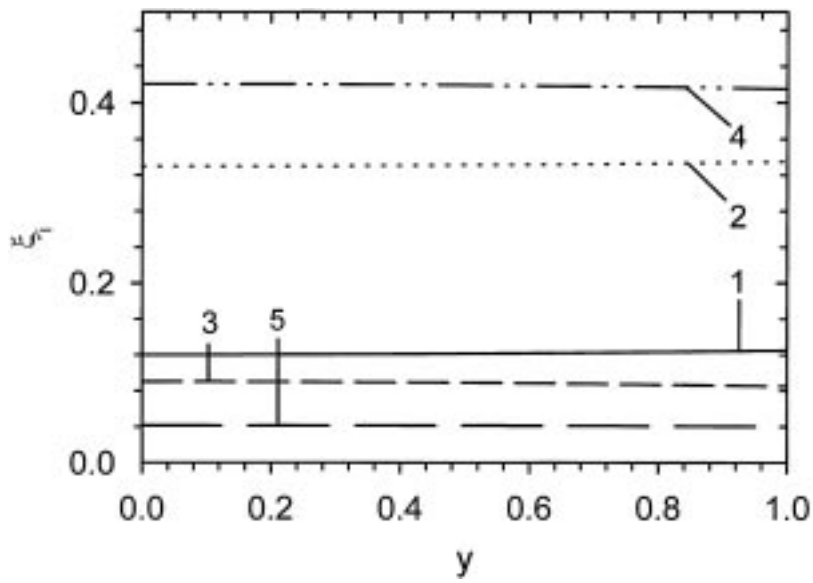

Fig. 11. Dimensionless partial pressures at $\delta = 2$. Parameters are the same as curve d in Fig. 7.

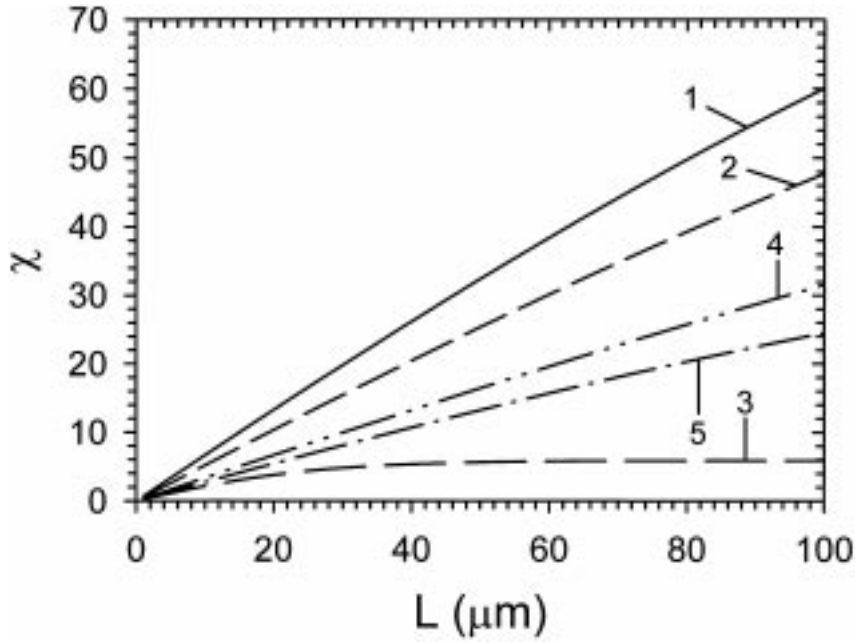

Fig. 12. Ratio χ of total rate of the reforming reaction to rate of electrochemical reaction (Eq. (64)) versus thickness L, for $I = 80\,\mathrm{mA\,cm^{-2}}$. Curve 1: Parameter set a, Table 2. Curve 2: Standard parameters, but with $\Phi = 0.4$. Curve 3: Standard parameters, but with porosity reduced to 0.04. Curve 4: Standard parameters, but with $\alpha = a_{el}/a_{ed} = 0.5$. Curve 5: Standard parameters. Partial pressures at $y = 1$ corresponds to $S/C = 2$ and $\Delta = 0.05$ for curves 1 through 4, and $S/C = 2$ and $\Delta = 0.5$ for curve 5. See text for details.

potential for none of the cases indicate significant power loss for thicknesses larger than roughly 10 μm, Fig. 13. Beyond a certain threshold, the potential is not very thickness dependent, although an increase with L for large L in the case with 4% porosity is apparent. The low porosity case also differs from the others in displaying much stronger pressure variations within the electrode. This is demonstrated by comparing Figs. 10 and 11 with Fig. 14, which shows ξ_i as functions of y for $\varepsilon = 0.04$ at 80 mA cm^{-2} for thickness $L = 50\,\mu$m.

More rigorous expressions for the fluxes of gas species than the Fick's law approach used in Eq. (15) above, may be found in the dusty-gas model (DGM) [52,62,79]. For an isothermal system, the DGM expression for N_i is

$$\sum_{j=1,j\neq i}^{n} \frac{y_i N_j - y_j N_i}{P D_{ij}^e} - \frac{N_i}{P D_{i,k}} = \frac{1}{RT}\frac{\partial y_i}{\partial x} + \frac{y_i}{PRT}\left(\frac{B_0 P}{\mu D_{i,k}^e} + 1\right)\frac{\partial P}{\partial x} \qquad (65)$$

where B_0 is a permeability coefficient, P the total pressure, y_i the mole fraction of species i, and μ the dynamic viscosity of the gas mixture. In Eq. (65), the second and third terms on the right-hand side represents viscous flow and pressure diffusion, respectively. In order to check Eq. (15) for consistency with the calculations, we calculated from Eq. (65) $\partial\xi_i/\partial y$ $(i = 1, \ldots, 5)$ using Eq. (15) for all N_i for a number of cases. In this calculation, the viscous flow terms was neglected in view of the results in Veldsink et al. [52]. For the parameter set of curve 1 of Fig. 12, $\partial\xi_1/\partial y$ calculated in this manner via Eq. (65) resulted in a value at $x = L$ roughly 30% off those in the figure. For all other $\partial\xi_i/\partial y$, the results were well within 10% of the model. Similar results were found for curves 2 and 4, whereas for curve 3 all $\partial\xi_i/\partial y$ were within 10%.

In addition to the calculation above, we also performed some using rate constants for the reforming reaction corresponding to the lower range of Table 2. As expected, the partial-pressure and reforming-rate variations were much smaller than for the corresponding cases with the higher value of k.

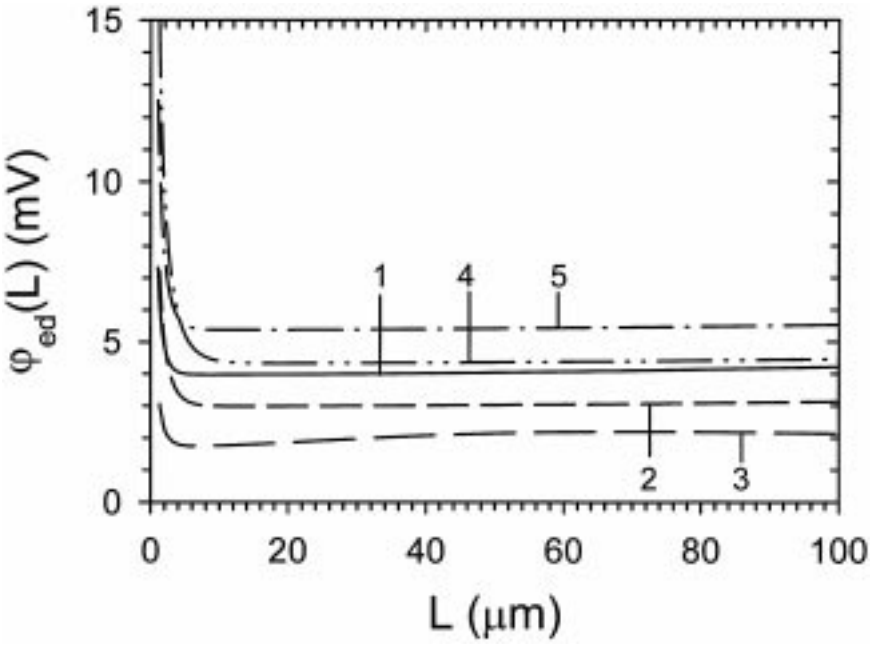

Fig. 13. Potential at the current collector, $\varphi_{ed}(L)$, versus electrode thickness L, for $I = 80\,\mathrm{mA\,cm^{-2}}$. Parameters as for the corresponding numbers of Fig. 12.

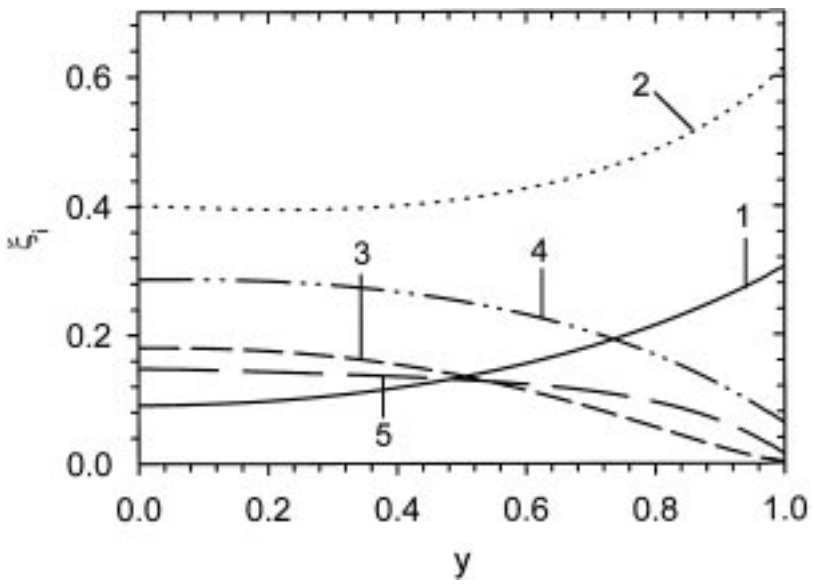

Fig. 14. Dimensionless partial pressures at $L = 50\,\mu$m for case 3 of Fig. 13.

Discussion

The gas-pressure variations along the pores in Figs. 10, 11 and 14 appears to be consistent with assumption 10, and partly also 4 and 7, made above. From the small variations in the total pressure along the pores (< 1% for Figs. 10 and 11, and < 3% for Fig. 14), the treatment of gas-phase transport as purely diffusive is presumably a very good approximation. The Fickian diffusion model for cases with larger pressure variations were discussed and compared with models including pressure diffusion and viscous flow [79] by [52], for boundary conditions of the same type as those employed here. In view of the accuracy with which the parameters of Table 2 are known, the simplified diffusion model does also for larger pressure variations than those found here appear to give reasonable results [52].

The results are also in line with the assumption of hydrogen as the only species of importance in the electrochemical reaction (assumption 7). The specific polarization conductance κ_p for the electrochemical oxidation of CO varies approximately as $(p_5/p_3)^{1/2}$ for low p_5/p_3 and as $(p_5/p_3)^{-1/2}$ for high p_3/p_5 [80], and is in the order of $10^{-4}\,\mathrm{S\,cm^{-1}}$ [80,81] at $p_3 = 0.333\,\mathrm{atm}$ and $p_5 = 0.667\,\mathrm{atm}$ [80,81]. (Older results also indicate qualitatively the same behavior of κ_p with p_3 and p_5 [54].) The partial-pressure variations along the pores therefore indicate that neglecting the electrochemical oxidation of CO is a good approximation, since the partial pressures of CO and CO_2 are low and the ratio between them is significantly different from unity [3,54,80]. The small variations in the ratio p_2/p_4 also indicates small variations in U', in line with assumption 10.

While assumption 5 is a matter of experimental arrangement and the assumptions underlying the macroscopic-electrode theory has been addressed above, the remaining assumptions can not be checked within the present framework. Of these, the most restricting one is probably assuming the rate of reaction (8) to be proportional to l_{TPB}. Recent modeling of this reaction at composite electrodes appear to indicate that this reaction would also depend to a certain extent on the surface area of particles [24]. No direct experimental evidence for this is yet available. However, we note that in case of a dependence of the electrochemical reaction rate on the areas of gas-solid interfaces, the increase in current-collector potential with reduced porosity may be larger than expected from Fig. 13. Also, in the latter case, using bulk conductivities instead of the prefactors of Eqs. (55) and (56) underestimates the overall resistance of the electrode. We also note that assumption 9 of isothermal operation improves the better the electrochemically produced heat balances the heat required by the reforming reaction. We therefore conclude that for the cases of most interest, the results are consistent with the assumptions made, as far as these are possible to check.

From Fig. 12, it appears that thickness is crucial in controlling χ for given microstructure and gas-phase composition. The accompanying loss in power, proportional to the increased current-collector potential, is negligible in most cases for thicknesses larger than $10\,\mu\mathrm{m}$ (Fig. 13). At large thicknesses, there even appears to be a small gain in power in reducing L in some cases, Fig. 13, notably curve 3 (see below). For a given thickness and gas composition, reducing Φ and ε, and using a coarser Ni network appears to have only a moderate effect on χ, Fig. 12, but a certain gain in $1/\chi$ might be expected from tuning these as well. In addition, the prereforming rate is important (Fig. 12), but this parameter would probably be dictated by considerations other than optimizing χ [50].

In a qualitative sense, the main conclusions above do not appear to be affected by the parameters known with less precision, like l_{TPB}, κ_p, γ_2 and γ_4 (Table 2), all connected to the electrochemical reaction. In particular, χ is not sensitive to the values of these for given current, due to the value of the parameter π_{12}. At atmospheric pressures, π_{12} is typically six orders of magnitude lower than π_{11} due to the large value of K_I. This means that the last term of the left-hand side of Eq. (30) can be omitted altogether. This decouples this equation from the remaining set, and the reforming rate becomes independent of the parameters for the electrochemical reaction. The overpotential and the current distribution, however, would be affected, Figs. 7 and 8. One should note that although the value of γ_4 appears particularly critical, the apparent reaction orders may affect the results in two ways. First, for given κ_p at given reference pressures, the reaction orders determine the extrapolated values of κ_p. Secondly, nonzero γ_2 and γ_4 imply that κ_p becomes a function of x as long as the partial pressures p_2 and p_4 are functions of x. However, from Figs. 10 and 11 the position dependence of the partial pressures is not

very strong. Therefore, the reaction orders are for most cases important only in the first, indirect sense, namely in determining the extrapolated values of κ_p (ν^2). Choices of κ_p and λ_{TPB} (or l_{TPB}) are discussed further in Sunde [19,22,23] and Mogensen et al. [38].

The thickness dependence of $\varphi_{ed}(L)$ seems to correlate well with the current distribution for corresponding parameter sets, c.f. Figs. 8 (set a) and 13 (curve 1). Since the current distribution is sensitive to γ_4 (Fig. 8), the exact thickness at which the overpotential becomes a strong function of thickness is also sensitive to γ_4, and will have to be ascertained experimentally.

We also note that the thickness dependence of the polarization resistance that can be inferred from Fig. 13 is qualitatively similar to that predicted by Eq. (1), except maybe for the lowest porosity.

From the results presented here, it does not appear that mass transfer is crucial in determining the key parameters χ and $\varphi_{ed}(L)$, except for very low porosity. In all other calculations, the pressure variations and the reforming rates are not strong functions of y, Figs. 9 through 11. In Fig. 13, the small increase in current-collector potential at large thicknesses may be ascribed to mass-transfer overpotential, however. (In principle, they could also be due to increased ohmic loss in the electrode. If this was the case, curve 3 of Fig. 13 should display the weaker L-dependence at large L compared to the other cases, due to the larger conductivities κ^*_{ed} and κ^*_{el}. As the opposite appears to be true, we dismiss the possibility of ohmic loss playing a significant role.) Also, in the complete absence of mass-transfer effects, the χ versus L relationships in Fig. 12 should be perfect straight lines. A slight bending at large L in curves 1, 2, 4, and 5, and a strong deviation from linearity in curve 3 indicate a small effect due to mass transfer in the first four cases, and a strong one in the latter, however. The surprisingly good accuracy of the simple estimates made in the introduction of this section may therefore be ascribed to rapid mass transfer at the temperatures relevant for SOFC operation and with the porosities common in SOFC electrodes so far. In most cases, Eq. (51) is a good approximation to the $\varphi_{ed}(L)$, which in conjunction with the solution of the simplified Eq. (30) may give an adequate description of both the electrochemical and reforming reactions.

Conclusions

In recent years, significant advances have been made in the understanding of composite electrodes for SOFC. In this, mathematical modeling and computer simulations have played a key role. In terms of ability to predict salient experimental features of composite electrode for SOFC, the Monte Carlo approach to modeling of such electrodes appears superior to the thin-film model and the macroscopic porous-electrode theory. Nevertheless, the latter represents a simplification that will give results in reasonable agreement with Monte Carlo calculations in a restricted parameter regime. As this regime is the one that happens to be the most interesting one for practical applications, the macroscopic approach should be useful in addressing engineering issues. Also, it appears more amenable for introducing non-linearities, gas-phase diffusion etc.

As an example of applying the theory for addressing a practical question, a model for the internal reforming rate of composite electrodes with concurrent electrochemical reaction was assembled. The calculations indicate that the parameter most important in controlling the ratio of the rate of methane reforming to that of the electrochemical oxidation of the reforming-reaction products at Ni-YSZ cermet anodes, is anode thickness. Particle size, volume fraction of Ni and porosity are less effective parameters in balancing the reaction rates. Unless porosity gets significantly lower than 30%, mass transfer in these electrodes is not important, rendering simpler estimates than the calculations performed here useful for prediction of anode behavior.

The example shows that a theory for composite fuel-cell electrodes that includes major features such as connectivity, gas-phase diffusion limitations, and non-linear electrochemical reactions can be simply assembled using the techniques described above.

Acknowledgments

Part of this work was performed under the Danish SOFC project, and sponsored by the Danish Ministry of Energy and by the Danish utility group ELSAM. The author wishes to acknowledge useful discussions with former coworkers Mogens Mogensen, Søren Primdahl, Peter Vang Hendriksen and Nicholas

Bonanos at Risø. An anonymous reviewer is acknowledged for bringing to my attention the work of [39]. Jürgen Fleig and Joachim Maier are acknowledged for comments on current constriction at three-phase boundaries.

List of Symbols

a_i	radius of particle of type i, μm or cm [Eq. (63)]
a_p	particle radius in a composite with uniform particle radii, μm
a	specific surface area of catalyst in the anode, cm^{-1}
A	superficial electrode area, cm^2
B	relative density for random packings of spheres
B_0	permeability coefficient, cm^2
D_{ij}^0	binary diffusion coefficient for species i and j, $\mathrm{cm}^2\,\mathrm{s}^{-1}$
D_{ij}^e	binary diffusion coefficient for species i and j in a porous medium with large pores, Eq. (54), $\mathrm{cm}^2\,\mathrm{s}^{-1}$
$D_{i,m}^e$	diffusion coefficient for species i in a gas mixture in a porous medium, $\mathrm{cm}^2\,\mathrm{s}^{-1}$
$D_{i,k}^e$	Knudsen diffusion coefficient multiplied by ε/τ, Eq. (54), $\mathrm{cm}^2\,\mathrm{s}^{-1}$
D_i^e	effective diffusion coefficient for species i in a gas mixture in a porous medium, $\mathrm{cm}^2\,\mathrm{s}^{-1}$
f_c	critical volume fraction of electrolyte particles
F	Faraday's number, 96485 C mol^{-1}
i_i	superficial current density in cluster of type i participating in an interface between two percolating clusters, $A\,\mathrm{cm}^{-2}$
i_0	exchange current per l_{TPB}, $A\,\mathrm{cm}^{-1}$
I	total superficial current density, $A\,\mathrm{cm}^{-2}$
I_i	sum of currents going into lattice site i, A^2
I_{ij}	current flowing through bond ij, A^2
j	dimensionless current density in percolating electrode clusters, i_{ed}/I
k	rate constant for the methane-reforming reaction, mol $\mathrm{s}^{-1}\,\mathrm{atm}^{-1}$
k_i	$k'_i r/2, \Omega\,\mathrm{cm}^3$
k'_i	interfacial resistance, Eq. (1), $\Omega\,\mathrm{cm}^2$
K_I	equilibrium constant for the reforming reaction, atm^2
K_{II}	equilibrium constant for the shift reaction
K_0	proportionality factor, Eq. (54) [52], cm
l	neck width, μm
l_{ij}	circumference of necks formed between particles i and j, μm
l_{TPB}	length of three-phase boundary, cm
L	electrode thickness, μm or cm [Eq. (1)]
M_i	molecular mass of species i, $\mathrm{kg\,mol}^{-1}$
n	number density of electrode particles, cm^{-3}
N_i	average flux density of species i, $\mathrm{mol\,cm}^{-2}\,\mathrm{s}^{-1}$
p	number fraction of electrode particles
p_k	number fraction of particles of type k
p^0	total pressure at $x = L$ atm
p_i	partial pressure of species i, atm
p_i^s	partial pressure of species i at $x = L$, atm
${p_i}^0$	reference pressure of species i, atm
P	total pressure, atm
P_c	percolation strength, Eq. (62)
r	pore radius, Eq. (1), cm, μm or m [Eq. (54)]
r_I, r_{II}	reaction rates of reactions (6) and (7), mol $\mathrm{cm}^{-2}\,\mathrm{s}^{-1}$
R	gas constant, $8.314\,\mathrm{J\,K}^{-1}\,\mathrm{mol}^{-1}$, $82.056\,\mathrm{cm}^3\,\mathrm{atm\,K}^{-1}\mathrm{mol}^{-1}$
R_p	polarization resistance, $\Omega\,\mathrm{cm}^2$
R_i	net production of species i per volume, $\mathrm{mol\,cm}^{-3}\,\mathrm{s}^{-1}$
S/C	steam-to-carbon ratio
t	critical exponent
T	temperature, K
U'	open-circuit potential, V
V_i	potential at site i in composite, V
x	coordinate normal to the anode plane, cm
x_i	mole fraction of species i
y	dimensionless coordinate, x/L
y_i	mole fraciton of species i
Z_t	total average coordination number
Z_i	interfacial impedance, Fig. 3
Z	dimensionless impedance
Z_j	total average coordination number for particles of type j
Z_{jk}	average number of k-neighbors of a particle of type j
Z_{ii}^c	average number of i-neighbors of a particle of type i at the percolation threshold for type-i particles
α	a_{el}/a_{ed}
β	β_c/β_a
β_a, β_c	potential parameters, Eq. (12), V^{-1}
γ_i	apparent reaction order for electrochemical reaction with respect to species i
Γ	$a_p/\cos[\tan^{-1}(1/2\pi a_p)]$, Eq. (2)
δ	dimensionless current, Eq. (45)
Δ	fraction of methane prereformed

ε porosity
η_s overpotential, V
κ conductivity ratio, Eq. (45)
κ_i bulk conductivity of the particles of type i, S cm^{-1}
κ_i^* effective conductivity of percolating cluster of i-particles in contact with a percolating cluster of the opposite kind, S cm^{-1}
κ_p specific electrocatalytic activity, S cm^{-1}
λ_{TPB} effective three-phase boundary length per volume, cm^{-2}
μ dynamic viscosity og gas mixture, atm s
ν square root of dimensionless exchange current density, Eq. (26)
ξ_i dimensionless partial pressure of species i
ξ_i^s dimensionless partial pressure of species i at $x = L$
π_{ij} dimensionless parameters, Eqs. (35) through (44)
ρ resistivity of electrolyte layer, Eq. (1), Ω cm
ρ_I dimensionless reforming reaction-rate, $d^2\xi_1/dy^2$
σ_i conductance of a bond between two electrode particles ($i =$ ''ed'') or two electrolyte particles ($i =$ ''el'') S
σ_{ij} conductance of bond between particles i and j S
σ_p polarization conductance for a bond between an electrode particle and an electrolyte particle S
τ tortuosity
χ ratio of the rate of the reforming reaction to $I/2F$
φ_i potential in cluster of type i participating in an interface between two percolating clusters, V
ϕ $\beta_a\eta_s$
Φ volume fraction of electrode particles
Φ_c critical volume fraction of electrode particles
ω angular frequency (Fig. 3), Hz

Subscripts
ed electrode particle
el electrolyte particle

References

1. L.E. Stoddard, in *Power Plant Engineering*, edited by L.F. Drbal, P.G. Boston, K.L. Westra and R.B. Erickson (Chapman & Hall, New York, 1996), p. 781.
2. A. Hammou, in *Advances in Electrochemical Science and Engineering* **2**, edited by H. Gerischer and C.W. Tobias (VCH, Weinheim, 1992), p. 87.
3. N.Q. Minh and T. Takahashi, *Science and Technology of Ceramic Fuel Cells* (Elsevier, Amsterdam, 1995).
4. D.W. Dees, T.D. Claar, T.E. Easler, D.C. Fee, and F.C. Mrazek, *J. Electrochem. Soc*., **134**, 2141 (1987).
5. T. Saito, in *Proc. 1991 IEA SOFC Workshop, Oslo, Norway, August 18–23*, edited by B. Thorstensen (Senter for Industriforskning, Oslo, 1991) p. 97. (b) T. Saito, in *SOFC Micromodelling* edited by L. Dubal (International Energy Agency, Bern, 1992) p. 21. (c) T. Saito, Y. Akiyama, N. Ishida, T. Yasuo, S. Taniguchi, S. Murakami and N. Furukawa, *Denki Kagaku*, **61**, 228 (1993).
6. T. Kawada, N. Sakai, H. Yokokawa, M. Dokiya, M. Mori, and T. Iwata, *J. Electrochem. Soc*., **137**, 3042 (1990).
7. T. Kawada, N. Sakai, H. Yokokawa, M. Dokiya, M. Mori, and T. Iwata, *Solid State Ionics*, **40/41**, 402 (1990).
8. W. Huebner, H.U. Anderson, D.M. Reed, S.R. Sehlin, and X. Deng, in *Solid Oxide Fuel Cells IV*, edited by M. Dokiya, O. Yamamoto, H. Tagawa and S.C. Singhal (**PV 95-1**, The Electrochemical Society Proceedings Series, Pennington, NJ, 1995), p. 696.
9. M. Mogensen and T. Lindegaard, in *Solid Oxide Fuel Cells* edited by S.C. Singhal and H. Iwahara (**PV 93-4**, The Electrochemical Society Proceedings Series, Pennington, NJ, 1993), p. 484.
10. M. Mogensen, in *High Temperature Electrochemical Behavior of Fast Ion and Mixed Conductors*, edited by F.W. Poulsen, J.J. Bentzen, T. Jacobsen, E. Skou, and M.J.L. Østergård (Proc. 14th Risø International Symposium on Materials Science, Risø 1993), p. 117.
11. M. Mogensen, S. Primdahl, J.T. Rheinländer, S. Gormsen, S. Linderoth, and M. Brown, in *Solid Oxide Fuel Cells IV*, edited by M. Dokiya, O. Yamamoto, H. Tagawa and S.C. Singhal (**PV 95-1**, The Electrochemical Society Proceedings Series, Pennington, NJ, 1995), p. 657.
12. M. Mogensen and S. Skaarup, *Solid State Ionics*, **86–88**, 1151 (1996).
13. T. Shirakawa, S. Matsuda, and A. Fukushima, in *Solid Oxide Fuel Cells* edited by S.C. Singhal and H. Iwahara, (**PV 93-4**, The Electrochemical Society Proceedings Series, Pennington, NJ, 1993), p. 464.
14. A. Tintinelli, C. Rizzo, G. Giunta, and A. Selvaggi, in *Proceedings of the 1st European SOFC Forum*, edited by Ulf Bossel, **1** (Lucerne, Switzerland, 1994), p. 455.
15. E. Ivers-Tiffé, W. Wersing, M. Schieß l, and H. Greiner, *Ber. Bunsenges. Phys. Chem*., **94**, 978 (1990).
16. I. Yasuda, T. Kawashima, T. Koyama, Y. Matsuzaki, and T. Hikita, *Proceedings of the International Fuel Cell Conference* February 3–6, 1992, Makuhari, Japan, 357 (1992).
17. T. Kenjo, S. Osawa, and K. Fujikawa, *J. Electrochem. Soc*., **138**, 349 (1991).
18. T. Kenjo and M. Nishiya, *Solid State Ionics*, **57**, 295 (1992).
19. S. Sunde, *J. Electrochem. Soc*., **142**, L50 (1995).
20. M. Juhl, S. Primdahl, C. Manon, and M. Mogensen, *J. Power Sources*, **61**, 173 (1996).
21. C.W. Tanner, K.-Z. Fung, and A.V. Virkar, *J. Electrochem. Soc*., **144**, 21 (1997).

22. S. Sunde, *J. Electrochem. Soc*., **143**, 1123 (1996).
23. S. Sunde, *J. Electrochem. Soc*., **143**, 1930 (1996).
24. S. Sunde, *Electrochimica Acta*, **42**, 2637 (1997).
25. P. Costamagna, P. Costa, and V. Antonucci, *Electrochimica Acta*, **43**, 375 (1997).
26. P. Costamagna, P. Costa, and E. Arato, *Electrochimica Acta*, **43**, 967 (1997).
27. H. Itoh, T. Yamamoto, M. Mori, T. Watanabe, and T. Abe, *Denki Kagaku*, **64**, 549 (1996).
28. J. Mizusaki, H. Tagawa, K. Tsuneyoshi, and A. Sawata, *J. Electrochem. Soc*., **138**, 1867 (1991).
29. M.J.L. Østergård, C. Clausen, C. Bagger, and M. Mogensen, *Electrochimica Acta*, **40**, 1971 (1995).
30. L.S. Wang and S.A. Barnett, *J. Electrochem. Soc*., **139**, 1134 (1992).
31. L.S. Wang and S.A. Barnett, *Solid State Ionics*, **76**, 103 (1995).
32. C.-H. Lee, C.-H. Lee, H.-Y. Lee, and S.M. Oh, *Solid State Ionics*, **98**, 39 (1997).
33. C.H. Bennett, *J. Appl. Phys*., **43**, 2727 (1972).
34. A.J. Matheson, *J. Phys. C: Solid State Phys*., **7**, 2569 (1974).
35. S. Kirkpatrick, *Rev. Mod. Phys*., **45**, 574, (1973).
36. D. Stauffer and A. Aharony, *Introduction to Percolation Theory* Revised 2nd ed. (Taylor & Francis, London, 1994).
37. S. Feng, B.I. Halperin, and P.N. Sen, *Phys. Rev. B*, **35**, 197 (1987).
38. M. Mogensen, S. Sunde, and S. Primdahl, in *High Temperature Electrochemistry: Ceramics and Metals*, edited by F.W. Poulsen, N. Bonanos, S. Linderoth, M. Mogensen, and B. Zachau-Christensen (Proc. 17th Risø International Symposium on Materials Science, Risø, 1996), p. 77.
39. J. Abel, A.A. Kornyshev, and W. Lehnert, *J. Electrochem. Soc*., **144**, 4253 (1997).
40. J. Fleig and J. Maier, *J. Electrochem. Soc*., **144**, L302 (1997).
41. J. Fleig and J. Maier, *J. Electroceramics*, **1**, 73 (1997).
42. J.S. Newman, *Electrochemical Systems* 2nd edition (Prentice-Hall, Englewood Cliffs 1991) (a) pp. 378–390, (b) pp. 454–469, (c) pp. 539–554.
43. D.S. McLachlan, M. Blaszkiewicz, and R.E. Newnham, *J. Am. Ceram. Soc*., **73**, 2187 (1990).
44. D. Bouvard and F.F. Lange, *Acta Metall. Mater*., **39**, 3083 (1991).
45. M. Suzuki and T. Oshima, *Powder Technology*, **35**, 159 (1983).
46. C.-H. Kuo and P.K. Gupta, *Acta Metall. Materialia*, **43**, 397 (1995).
47. E. Achenbach and E. Riensche, *J. Power Sources*, **52**, 283 (1994).
48. K. Aasberg-Petersen, in *Proceedings of the 1st European SOFC Forum*, edited by Ulf Bossel, **1** (Lucerne, Switzerland, 1994), p. 111.
49. P.S. Christensen, in *Abstracts, 7th IEA SOFC Workshop Theory and Measurement of Microscale Processes in Solid Oxide Fuel Cells*, (Wadahl, Norway, January 18–20, 1995), p. 95.
50. E. Achenbach, *J. Power Sources*, **49**, 333 (1994).
51. R. Ødegård, E. Johnsen, and H. Karoliussen, in *Solid Oxide Fuel Cells IV*. edited by M. Dokiya, O. Yamamoto, H. Tagawa and S.C. Singhal (**PV 95-1**, The Electrochemical Society Proceedings Series, Pennington, NJ, 1995), p. 810.
52. J.W. Veldsink, R.M.J. van Damme, G.F. Versteeg, and W.P.M. van Swaaij, *Chem. Eng. J*., **57**, 115 (1995).
53. B.C. Nguyen, T.A. Lin, and D.M. Mason, *J. Electrochem. Soc*., **133**, 1806 (1986).
54. T.H. Etsell and S.N. Flengas, *J. Electrochem. Soc*., **118**, 1890 (1971).
55. S.V. Karpachev, A.E. Zupnik, and M.V. Perfil'ev, *Soviet Electrochem*., **6**, 443 (1970).
56. V.D. Belyaev, T.I. Politova, O.A. Mar'ina, and V.A. Sobyanin, *J. Catalysis A: General*, **133**, 122 (1996).
57. T. Norby, O.J. Velle, H. Leth-Olsen, and R. Tunold, in *Solid Oxide Fuel Cells* edited by S.C. Singhal and H. Iwahara (**PV 93-4**, The Electrochemical Society Proceedings Series, Pennington, NJ, 1993), p. 473.
58. E.J.L. Schouler and H.S. Isaacs, *Solid State Ionics*, **5**, 555 (1981).
59. J. Mizusaki, H. Tagawa, T. Saito, K. Kamitani, T. Yamamura, K. Hirano, S. Ehara, T. Takagi, T. Hikita, M. Ippomatsu, S. Nakagawa, and K. Hashimoto, *J. Electrochem. Soc*., **141**, 2129 (1994).
60. H.S. Isaacs and L.J. Olmer, *J. Electrochem. Soc*., **129**, 436 (1982).
61. J.S. Newman and C.W. Tobias, *J. Electrochem. Soc*., **109**, 1183 (1962).
62. M.E. Abashar and S.S. Elnashaie, *Mathl. Comput. Modeling*, **18**, 85 (1993).
63. A.L. Lee, R.F. Zabransky, and W.J. Huber, *Ind. Eng. Chem. Res*., **29**, 766 (1990).
64. A. Solheim, in *Proc. 1991 IEA SOFC Workshop* Oslo, Norway, August 18–23, edited by B. Thorstensen (Senter for Industriforskning, Oslo, 1991), p. 75.
65. U.G. Bossel, *Facts and Figures* (Final Report on SOFC Data to the International Energy Agency Bern 1992), p. B19.
66. R.B. Bird, W.E. Stewart, and E.N. Lightfoot, *Transport Phenomena* (John Wiley and Sons, New York, 1960), p. 505.
67. D.S. Bordreaux and J.M. Gregor, *J. Appl. Phys*., **48**, 152 (1977).
68. J. Rodriguez, C.H. Allibert, and J.M. Chaix, *Powder Technol*., **47**, 25 (1986).
69. S. Murukami, Y. Akiyama, N. Ishida, T. Yasuo, T. Saito, and N. Furukawa, in *Proc. 2nd International Symposium on SOFC, 2 – 5 July 1991, Athens, Greece*, edited by F. Gross, P. Zegers, S.C. Singhal and O. Yamamoto (Athens, 1991), p. 105.
70. *Thermophysical Properties of High Temperature Solid Materials*, edited by Y.S. Touloukian, **I** (Macmillan, New York, 1967), p. 696.
71. T. Yamamura, H. Yoshitake, H. Tagawa, N. Mori, K. Hirano, J. Mizusaki, S. Ehara, T. Takagi, M. Hishinuma, H. Sasaki, Y. Nakamura, and K. Hashimoto, in *Proceedings of the 2nd European SOFC Forum*, edited by Bernt Thorstensen, **2** (Oslo, Norway, 1996), p. 617.
72. J.R. Rostrup-Nielsen, *Steam Reforming Catalysts* (Danish Technical Press Inc., Copenhagen, 1975), p. 24.
73. N. Nakagawa, H. Sakurai, K. Kondo, T. Morimoto, K. Hatanaka, and K. Kato, *J. Electrochem. Soc*., **142**, 3474 (1995).
74. T. Yamamura, H. Tagawa, T. Saito, J. Mizusaki, K. Kamitani, K. Hirano, S. Ehara, T. Takagi, Y. Hishinuma, H. Sasaki, T. Sogi, Y. Nakamura, and K. Hashimoto, in *Solid Oxide Fuel Cells IV*, edited by M. Dokiya, O. Yamamoto, H. Tagawa and S.C. Singhal, (**PV 95-1**, The Electrochemical Society Proceedings Series, Pennington, NJ, 1995), p. 741.

75. J. Mizusaki, H. Tagawa, T. Saito, T. Yamamura, K. Kamitani, K. Hirano, S. Ehara, T. Takagi, T. Hikita, M. Ippomatsu, S. Nakagawa, and K. Hashimoto, *Solid State Ionics*, **70/71**, 52 (1994).
76. T. Norby, in *Proceedings of the 2nd European SOFC Forum* edited by Bernt Thorstensen, **2** (Oslo, Norway, 1996), p. 607.
77. J. Guindet, C. Roux, and A. Hammou, in *Proc. 2nd International Symposium on SOFC*, 2–5 July 1991, Athens, Greece, edited by F. Gross, P. Zegers, S.C. Singhal and O. Yamamoto (Athens, 1991), p. 553.
78. J.N. Roberts and L.M. Schwartz, *Phys. Rev. B*, **31**, 5990 (1985).
79. E.A. Mason, A.P. Malinauskas, and R.B. Evans, *J. Chem. Phys.*, **46**, 3199 (1967).
80. G.Ø. Lauvstad, *Electrochemistry of the CO-CO_2 system on solid electrolytes (Dr. ing. thesis 1996:52, The Norwegian Institute of Technology, Trondheim, Norway, 1996).*
81. G.Ø. Lauvstad, S. Sunde, and R. Tunold, in *High Temperature Electrochemistry: Ceramics and Metals*, edited by F.W. Poulsen, N. Bonanos, S. Linderoth, M. Mogensen, and B.